Innovative Desalination System Driven by a Solar Micro Gas Turbine for Off-Grid Applications

Rafael González-Almenara, Lourdes García-Rodríguez, Antonio Muñoz, Tomás Sánchez, David Sánchez*

Department of Energy Engineering, University of Seville, Camino de los descubrimientos s/n, 41092 Seville, Spain.

Abstract

Past work by the authors has suggested that Solar micro Gas Turbines (SmGTs) can be used cost-effectively to produce electric power and heat for freshwater production through desalination, mainly in off-grid locations. This is further studied in this work, presenting a detailed description of system performance at design and part-load conditions, as well as the characteristics of the components of the SmGT and the desalination unit. To this end, the SmGT is assessed first, considering techniques that achieve a greater off-design performance such as incorporating Variable Inlet Guide Vanes (VIGVs) at the compressor inlet, and including the sensitivity to control strategies and ambient conditions, exploring their expectedly very negative impact on the SmGT performance. Water treatment system is comprised of two elements. A Reverse Osmosis desalination unit is driven by the electric power produced by the SmGT. This produces brine with high salt concentration to be partially treated further in a Zero Liquid Discharge (ZLD) unit driven by the exhaust gases of the microturbine (at about 250-300ºC), where the sensible heat of this stream is harvested by the ZLD unit to "dry" and concentrate the effluent. Finally, the potential and the operational limitations of the ZLD system are discussed, supplemented by an experimental proof of concept where its feasibility was verified.

Keywords: SOLMIDEFF, Solar Micro Gas Turbine, Microturbine, Desalination, ZLD

Nomenclature

Δ_z	Rotor Axial Length	$[m]$
$\dot{C}_i^*$	Ratio of Heat Capacities	$[-]$
$\dot{m}$	Mass Flow Rate	$[kg/s]$
η	Efficiency	$[-]$
ν	Kinematic Viscosity	$[m^2/s]$
Ω	Total Pressure Loss Coefficient	$[-]$
ω_λ	Abrupt Expansion Losses	$[-]$
ω_{BL}	Blades Losses	$[-]$
ω_{CH}	Aerodynamic Blockage Losses	$[-]$
ω_{cl}	Clearance Losses	$[-]$
ω_{cr}	Supercritical Mach Number Losses	$[-]$

*Corresponding author. Tel.: +34 954 487 241.

Email addresses: rgalmenara@us.es (Rafael González-Almenara), mgarcia17@us.es (Lourdes García-Rodríguez), ambl@us.es (Antonio Muñoz), tmsl@us.es (Tomás Sánchez), ds@us.es (David Sánchez)

ω_{dif} Entrance Diffusion Losses $[-]$

ω_{HS} Hub-to-Shroud Loading Losses $[-]$

ω_{inc} Incidence Losses $[-]$

ω_{mix} Mixing Losses $[-]$

ω_{sf} Skin Friction Losses $[-]$

ϕ Flow Coefficient $[-]$

Π Osmotic Pressure $[bar]$

ψ Work Coefficient $[-]$

ε Effectiveness $[-]$

b_{in} Rotor inlet passage width $[m]$

C_d Discharge Coefficient $[-]$

d Solar Receiver Nozzle Diameter $[m]$

D_{cav} Cavity Diameter $[m]$

F Feed $[-]$

I Work Input Coefficient $[-]$

I_{bl} Blade Loading Losses $[-]$

I_{df} Disk Friction Losses $[-]$

I_{leaf} Leakage Losses $[-]$

I_{recir} Recirculation Losses $[-]$

j Solar Receiver Nozzle rows $[-]$

k_{wf} Thermal Conductivity of the Working Fluid $[W/(m \cdot K)]$

m_{bi} Brine Inlet Mass Flow Rate $[kg/s]$

m_{bo} Brine Outlet Mass Flow Rate $[kg/s]$

m_{gi} Gases Inlet Mass Flow Rate $[kg/s]$

N Total Number of sub-Heat Exchangers $[-]$

n Total number of Solar Receiver nozzles $[-]$

n_s Specific Speed $[-]$

P Permeate $[-]$

$p\prime_t$ Total Pressure $[-]$

P_{jet} Jet Pitch $[m]$

q_v Volumetric Flow Rate $[m^3/s]$

r_V Recovery Rate $[-]$

S Salinity $[kg/kg]$

S_{bi} Brine Inlet Salinity $[kg/kg]$

S_{bo} Brine Outlet Salinity $[kg/kg]$

T_{bi} Brine Inlet Temperature $[K]$

T_{bo} Brine Outlet Temperature $[K]$

T_{gi} Gases Inlet Temperature $[K]$

U Global Heat Exchange Coefficient $[W/(m^2 \cdot K)]$

v_s Total-to-Total Velocity Ratio $[-]$

Y_{BL} Blade Loading Losses $[-]$

Y_{cl} Clearance Losses $[-]$

Y_{HS} Hub-to-Shroud Losses $[-]$

Y_{inc} Incidence Losses $[-]$

Y_p Profile Losses $[-]$

Y_Q Moisture Losses $[-]$

Y_{rot} Rotor Loss Coefficient $[-]$

BB Billion Barrels $[-]$

BCF Billion Cubic Feet $[-]$

BD BlowDown $[-]$

BP Booster Pump $[-]$

CHP Combined Heat and Power $[-]$

CSP Concentrated Solar Power $[-]$

DNI Direct Normal Irradiance $[W/m^2]$

ERD Energy Recovery Device $[-]$

GDP Gross domestic product $[-]$

HDH Humidification-DeHumidification $[-]$

HPP High Pressure Pump $[-]$

ICE Internal Combustion Engine $[-]$

ICH Isobaric Chamber $[-]$

MD Membrane Distillation $[-]$

MED Multi-Effect Distillation $[-]$

mGT Micro Gas Turbine $[-]$

MSF Multi-Stage Flash $[-]$

ORC	Organic Rankine Cycle	$[-]$
PR	Pressure Ratio, Performance Ratio	$[-]$
Pr	Prandtl Number	$[-]$
PSHE	Primary Surface Heat Exchanger	$[-]$
PTC	Parabolic-Trough Collector	$[-]$
PV	PhotoVoltaic	$[-]$
RO	Reverse Osmosis	$[-]$
SmGT	Solar Micro Gas Turbine	$[-]$
SSC	Stationary Solar Collector	$[-]$
SWRO	SeaWater Reverse Osmosis	$[-]$
TDS	Total Dissolved Solids	$[ppm]$
TIT	Turbine Inlet Temperature	$[K]$
TOT	Turbine Outlet Temperature	$[K]$
TVC	Thermal Vapour Compression	$[-]$
UA	Conductance	$[W/K]$
VIGV	Variable Inlet Guide Vanes	$[-]$
VNGV	Variable Nozzle Guide Vanes	$[-]$
ZLD	Zero Liquid Discharge	$[-]$

1. Introduction

1.1. Background

This paper presents the technical details of an innovative integrated system aimed at enabling a large reduction of the carbon footprint of water desalination in areas currently subjected to extreme water scarcity, in particular the Middle East and Northern Africa. In these regions, the characteristic boundary conditions include a very high available solar resource and also large regions where the grid is not available. Therefore, the conditions to integrate solar power generation and water desalination are met, in an attempt to tackle not only water scarcity but also a heavy reliance on fossil fuel for electricity supply.

The countries in the Middle East have almost 50% of the world reserves of crude oil and they can be categorised in two main groups. On the one hand, certain countries in the Middle-East with very high state and individual wealth (gross GDP and GDP per capita), mostly affiliated with the Gulf Cooperation Council (Saudi Arabia, Kuwait, Qatar,United Arab Emirates and, to a lesser extent, Oman and Bahrain) and accounting for over 30% of the world reserves of crude oil; these countries have seen a remarkable economic growth, as a consequence of which the energy consumption per capita has rocketed not only for the increased demand but also for certain policies discouraging an efficient use of energy (for instance, through subsidised energy prices). On the other hand, certain countries also in the Middle East (Iran, Irak) and in Northern Africa (Libya, Algeria) which have not seen a similar improvement of the individual wealth despite their large share of oil reserves (15-20%). When natural gas and not oil is considered, the situation is somewhat similar even if the numbers add differently. Overall, regardless of the different characteristics of these two groups of countries, they share a strong dependence on fossil fuels to cover the power needs (>95% of the electricity comes from natural gas or coal, 100% in several cases) [1, 2]. All this information is shown in Table 1.

Country	Consumption of Electricity [kWh/person·year]	Fossil Fuels Energy mix [%]	Water Availability [m^3/person·year]	Oil Reserves [BB]	Oil Reserves [%]	GDP per capita [USD_{2010}]	Natural Gas Reserves [BCF]	Natural Gas Reserves [%]
Algeria	1363	99	272.3	12.2	0.69	4710.6	159054	2.3
Bahrain	19597	99.7	2.679	0.09	0.01	20913	3250	0.05
Egypt	1683	90	10.25	3.3	0.19	3008.8	77200	1.1
Iran	3022	92.7	1583	155.6	8.74	5627	1201382	17.3
Iraq	1328	95.5	919.7	145.02	8.15	4837.4	111522	1.6
Kuwait	15591	100	0	101.5	5.70	32697.3	63500	0.9
Libya	1811	100	109.8	48.36	2.72	8122.2	58183	0.8
Morocco	904	84.6	811.4	0	0.00	3396.1	51	0
Oman	6446	100	302	5.37	0.30	14992.6	24910	0.4
Qatar	14792	100	21.22	25.24	1.42	62021.1	871585	12.5
Saud Arabia	9401	100	72.86	267.03	15.00	20542.2	294205	4.2
UAE	11088	100	15.96	97.8	5.50	41420.5	215098	3.1
Yemen	220	98	74.34	3	0.17	0	16900	0.2

Table 1: Energy, economic and water related indicators of selected countries in the MENA region [1, 2]. Oil and Natural Gas reserves are given in billion barrels [BB] and billion cubic feet [BCF] (2019 data).

The aforedescribed abundance of fossil fuels is in contrast with a low availability of water resources, in most cases well below the water poverty or absolute water poverty lines, 1000 and 500 m^3/(person· year) respectively, below which water becomes a primary constraint for human life. In some extreme cases, water availability is even below 100 m^3/(person· year), a limit that poses a very large and pressing threat for the sustainability of future generations. This is also shown in Table 1.

In the light of the situation above, it is now agreed that this environmental emergency must be tackled simultaneously for water and energy, exploiting the evident synergies between these two human needs and the abundant solar resource in the region. The current landscape for large-scale water technologies in this part of the world is characterised by large-capacity thermal desalination plants using technologies based on Multi-Effect Distillation (MED) or Multi-Stage Flash (MSF) integrated into thermal power plants, installed in the 20^{th} century for the most part but already obsolete in present times as a result of the superior performance of Reverse Osmosis (RO). At the smaller-scale and for off-grid installations, RO powered by photovoltaic panels seems to be the preferred option despite its disadvantages, since these systems typically require: i) backup generators burning fossil fuels to enable operation in the absence of solar energy, and ii) batteries to run the system overnight if needed. Such redundancy is, of course, less reliable and has higher capital and O&M costs than a single, flexible system.

This work introduces a technical solution which can possible tackle the flaws of PV-RO systems mentioned in the foregoing paragraph, producing freshwater with a single system able to work on solar energy and on backup fossil fuels whilst also reducing the liquid effluent from the water production process (i.e., lower environmental impact). This system is based on the coupling of a solar dish collector and a micro gas turbine, downstream of which water is produced in an RO unit driven by the electric power produced by the gas turbine system. A Zero Liquid Discharge (ZLD) system running on the available thermal energy of the exhaust of the gas turbine evaporates water from the concentrate, hence ensuring lower water content in the latter and, accordingly, lower environmental impact. Although no commercial systems have been installed so far, the techno-economic viability of Solar micro Gas Turbines (SmGT) has been addressed in literature, finding better-than-expected results in all aspects [3–7] and with the experimental support of a demonstrator installed at ENEA Research Centre (Italy) within the framework of the OMSoP project [8], funded by the European Commission. This system demonstrated the technical feasibility of the coupling of a solar dish collector and a micro gas turbine.

1.2. Scope of work and objectives

Micro Gas Turbines (mGT) are compact engines for on-site power and heat generation able to achieve electrical efficiencies between 15% (small engines of ~3 kWe [9]) and 40% (larger engines with unit output of ~400 kWe [10]) at full load and an overall energy utilisation of more than 90% in Combined Heat and Power (CHP) configuration [9]. A mGT includes the following components: compressor, turbine/expander, combustor, recuperator, fuel supply system, bearings (most commonly with an associated lube oil system), electric generator, power conditioning and control unit, enclosure and balance-of-plant. Some of these components might not be present in a particular mGT, as this depends on the type of application such as the solar micro gas turbines where a solar receiver replaces the combustor.

Although market for decentralised, micro energy systems is currently dominated by reciprocating Internal Combustion Engines (ICE), micro gas turbines are reportedly competitive against ICEs in applications requiring intermediate to high-grade heat and high heat-to-power ratio [11]. The micro gas turbines in these applications exhibit some variations with respect to large gas turbines, the utilisation of radial machinery being the most relevant feature. In micro gas turbines, single-stage radial compressors are standard and this limits the pressure ratio of the engine to values not higher than 4 (approximately). On the other hand, the utilisation of radial expanders prevents the use of blade cooling and this, in turn, limits Turbine Inlet Temperature (TIT) to values lower than 950ºC. Both pressure ratio and turbine inlet temperature are significantly lower than in large gas turbines, what brings about a dramatic efficiency drop if simple Brayton cycles are used. Accordingly, micro gas turbines typically adopt recuperative cycle layouts in order to increase thermal efficiency to more competitive values [12].

Further to the aforecited potential of micro gas turbines for decentralised power, in particular applied to renewable energy sources, and based on the past experience of the authors, a solar desalination system based on SmGTs with the techno-economic features already presented in [13–15] seems to be a cost-effective solution with a promising future against other popular renewable desalination options integrating PV panels. This has already been explored for isolated units [16] but, according to recent literature on the topic, it might also apply to larger scales by coupling several SmGTs in parallel.

The main features of the solar desalination arrangement proposed are:

- The high temperature available at the turbine exhaust has the potential to drive thermal desalination processes based on phase change. In this case, the permeate of an upstream RO process could be blended with the distillate produced by distillation in order to increase the quality of the fresh water produced. Another option would be to direct the concentrate of the RO unit to a thermal ZLD system were the total water content of the effluent could be reduced, thereby minimising the environmental impact of water desalination.
- Biofuels can be used as a back-up energy source to maintain the system operating at full capacity 24/7 and to compensate for cloudy/hazy sky conditions. This avoids the usual oversizing of desalination systems typically required in solar applications in order to achieve reasonable capacity factors. Moreover, this oversizing brings about higher costs that challenge the economics of the systems and stem as the main economic hurdle for the development of solar desalination technologies.
- In parabolic dish systems, the integrated concentrator-receiver system can reach efficiencies as high as 80%. Then, the complete assembly with a mGT can potentially attain annual solar-to-electric efficiencies of 18.3%, when turbine inlet temperature is in the order of 850ºC. [17]. This is very close to the rated efficiency of approx 20%, or even more if a higher turbine inlet temperature is considered [5], which is similar to the efficiency of conventional, larger CSP plants. This ensures interesting market prospects of the technology when fully developed [7].

In order to justify the interest of this work, Fig. 1 presents a comparison of the expected efficiency achieved by different solar desalination technologies in terms of estimated solar energy required [kWh] to produce 1 m^3 of freshwater. The following technologies are considered:

- Five collector technologies: i) Stationary Solar Collectors (SSC), ii) Parabolic Trough Collectors (PTC), iii) heliostats, iv) Dish collectors and v) PV panels.
- Two thermo-mechanical energy conversion technologies: Organic Rankine Cycle systems (ORC) and micro Gas Turbines (mGT).
- Four desalination technologies based on phase-change: i) Membrane Distillation (MD), ii) Multi-Effect Distillation (MED), iii) MED with Thermal Vapour Compression (MED-TVC) and iv) Humidification-DeHumidification (HDH) with values of Performance Ratios (PR) taken from recent bibliography on the topic [18, 19].
- Desalination based on membrane technology: SWRO desalination with a specific energy consumption of 2.2 kWh/m^3 (as reported in recent literature on the topic [20]).

From the comparison in Fig. 1, the interest of the proposed solution in terms of specific energy consumption becomes evident. Therefore, a more detailed, in depth analysis is needed to verify if the performance reported in the char is actually accurate.

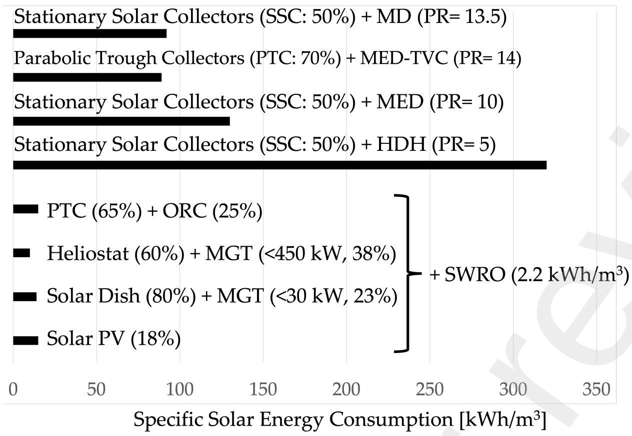

Figure 1: Comparison of solar desalination based on reverse osmosis and phase change desalination. Estimates of energy efficiency of solar energy technologies are given in brackets along with that of power cycles [20].

2. System Description and Methodology

The system integrating the solar mGT and water treatment systems proposed, namely reverse osmosis desalination and ZLD, has been developed conceptually in the SOLMIDEFF project. This project, entitled *SOLar Micro gas turbine-driven Desalination for Environmental oFF-grid applications*, was developed by the research team at University of Seville, Spain, with funding from the National R&D programme of the Ministry of Science and Innovation. The reference site for the techno-economic assessment of the technology is in the Canary Islands.

The SOLMIDEFF system is based on a 10 kWe SmGT producing electric power and heat to run a desalination unit in off-grid applications. The desalination unit is comprised of a SWRO unit, driven by the electric power produced by the engine, and the Zero Liquid Discharge making use of the available gas in the exhaust from the SmGT. A schematic of the SOLMIDEFF system is presented in Fig. 2, where the three main subsystems (SmGT, SWRO and ZLD) are easily identified. A parabolic dish collects and concentrates solar energy onto a solar receiver where a large fraction of this concentrated solar power is absorbed by the working fluid of an open-cycle recuperated mGT, achieving a solar-to-electric efficiency of almost 20%. In this micro gas turbine, atmospheric air is compressed to 3.5 bar by a radial compressor and then heated up to 500ºC by a recuperative heat exchanger. The energy source for this temperature rise is the stream of hot gases flowing out from the turbine. After pressurisation and preheating, air flows into a solar receiver where it achieves a turbine inlet temperature of 850ºC thanks to the concentrated solar energy absorbed. If this were not possible, because of a lack of solar energy supply (hazy sky or, maybe, operation at night), a combustor in series or parallel with the receiver would be able to burn fuel in order to ensure power and water supply. Regardless of the energy source used to take the hot air to the target turbine inlet temperature, the hot pressurised gas is then expanded across the turbine which, in turns, produces power to drive the compressor and electric generator.

The electric power produced by the SmGT is used by a Reverse Osmosis plant, whose feed stream is seawater, brackish water or industrial wastewater. The particular arrangement of pumps and pressure exchange devices is shown in Fig. 2. The feed stream is split into two flows. One of them is sent to the high-pressure pump (HPP) where pressure is increased to 55 bar approximately. The remainder of the feed flow is sent to an isobaric chamber (ICH) where pressure is also increased thanks to the high pressure available at the outlet concentrate stream of the RO unit. In an energy recovery device (ERD) such as an ICH, volumetric flow rates on both sides are similar and the feed outlet pressure (stream 14) is slightly lower than the concentrate inlet pressure (stream 18) [21]. This pressure loss comes about because the ERD is not ideal and there are energy losses preventing a perfect match of the energy exchange

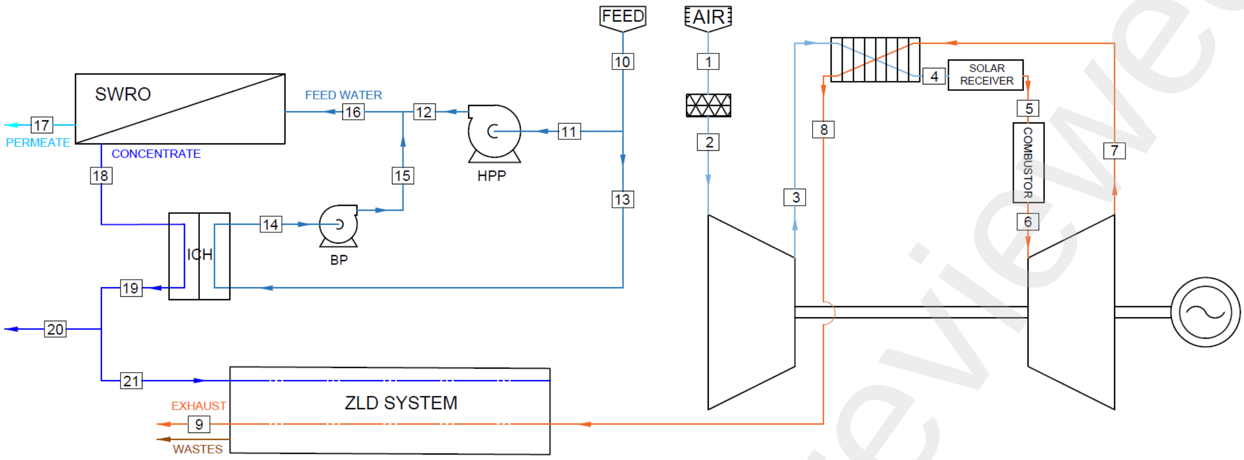

Figure 2: Schematic of the SmGT-driven desalination system (SOLMIDEFF system)

across the interacting streams; accordingly, a booster pump is needed downstream of the ERD (feed flow side) to make up for the pressure difference between the outlet from the ERD and the outlet from the HPP (inlet to the RO unit), as well as for the pressure drop through the membrane rack.

The concentrate flows across the energy recovery device, where pressure decreases to almost atmospheric. A fraction of this stream is then sent to the ZLD unit, where part of the water content evaporates thanks to the thermal energy available in the exhaust gases of the micro gas turbine. The ZLD unit is a direct-contact heat exchanger whose purpose is to reduce the amount of water released for disposal [16].

The methodology followed to model the design and performance of the SOLMIDEFF system is based on an integrated design and simulation platform which combines the design and off-design performance of each SOLMIDEFF component. The individual models have been implemented in Matlab enironment [22] and are solved through a modular approach which relies on the conservation of mass, energy and momentum and on set correlations to estimate energy losses and irreversibility of the individual components.

The working fluid of the SmGT is air (dry real gas) whose thermodynamic properties are obtained from Coolprop [23]. Once the simple recuperated Brayton cycle is resolved for a given set of boundary conditions (i.e., the pressure ratio yielding maximum net efficiency is calculated), one dimensional (1-D) models are used to produce efficient and flexible turbomachinery designs (compressor and turbine) whilst non-dimensional (0-D) approaches are used to design the recuperator and solar receiver. The final step to completely model the SmGT is to evaluate the off-design performance of the engine; this is driven by compressor-turbine matchning, which is implemented by a proprietary code making use of the methodology described by Razak [24]. In addition, several control strategies are embedded to ensure the safe operation of the SmGT in different load ranges and operating conditions.

The performance of the RO system for the treatment of industrial effluents and brackish or seawater has been modelled through well-known equations from literature [25], compiled in a block model callibrated against the software *Q+* developed by LG Chem [26]. finally, still within the water treatment subsystem, the proof-of-concept ZLD unit has been experimentally demonstrated for this application, and the associated model has already been published by the authors [16].

3. System Modelling and Performance

This section introduces the main features of the models used to characterise each main component of the SOLMIDEFF system. This includes the designs models as well as the models used to estimate off-design performance. The following subsystems are included: i) solar Micro Gas Turbine (compressor, solar subsystem, turbine/expander and recuperator), ii) SWRO system, and iii) ZLD system. Comments on the validation or verification of each of these models are also provided.

3.1. Solar Micro Gas Turbine

3.1.1. Compressor

The design and performance model of the centrifugal compressor is of the one-dimensional, mean-line type and it is based on Aungier´s works [27]. The design process begins from the work (ψ) and flow (ϕ) coefficients, target pressure ratio and mass flow rate, along with the specific ambient conditions of the reference locations. This standard approach, widely used in literature, is based on a stepwise methodology where the compressor elements are designed independently through non-dimensional coefficients (pressure losses and work input) along the meridional coordinate: impeller, diffuser and volute. Since the outlet conditions from the machine are required to estimate these coefficients, this methodology renders an iterative process whose design flowcharts are shown in Figs. 3-4. In the latter flowchart, blade loading (BL) is defined by Eq. 1.

$$BL = \frac{2\,\Delta W}{W_1 + W_2} \tag{1}$$

where ΔW represents the average blade velocity difference, used to estimate the number of blades of the impeller, and W_1 and W_2 is the relative flow velocity at impeller inlet and outlet.

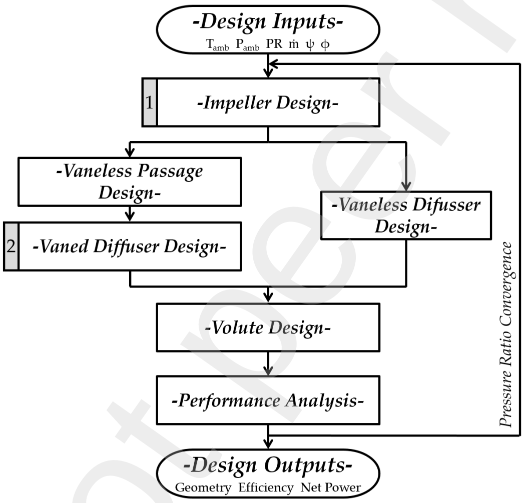

Figure 3: Compressor design flowchart.

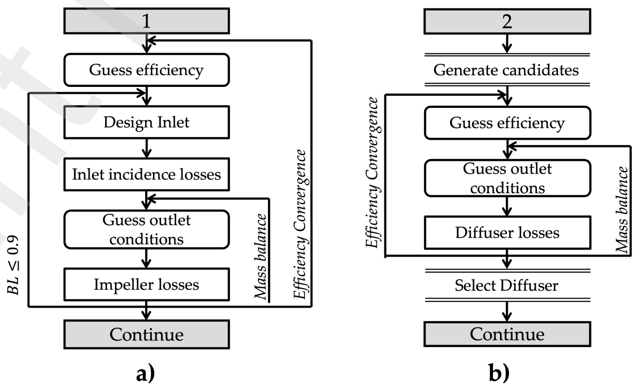

Figure 4: a) Impeller design flowchart and b) Vaned diffuser design flowchart.

Single stage compressors are considered by default, given the low pressure ratio of this type of engines (owing to the recuperative cycle layout), most often with full-inducer impellers. The blades are three-dimensional, based on straight-line surface elements that connect hub and shroud. The flow at the inlet is assumed axial with uniform flow distribution, with the variable inlet guide vanes (VIGV) set in the axial direction at the design point[1]. The meridional plane at the hub is constructed with the largest circular-arc possible (including linear extensions for the hub and shroud contours if needed) by specifying the slopes and coordinates of the impeller eye and tip. The contour of the shroud is defined on the other hand by a power-law linking the radial and axial coordinates.

The performance of the compressor is estimated from correlations modelling the internal flow physics and main loss mechanisms. For both, variations and corrections with respect to the original work by Aungier [27] have been introduced with the aim to obtain more accurate estimates. In particular: i) the slip factor is calculated from Wiesner correlation [28]; ii) the pressure loss coefficient across the Variable Inlet Guide Vanes is obtained as described by Japikse [29]; iii) leakage flows are calculated according to the work by Egli [30]; and iv) disk friction losses at the endwalls are estimated as suggested by Daily and Nece [31]. Incorporating all these losses, the total pressure and enthalpy at impeller outlet is determined by Eqs.(2-5):

$$p'_{t,2} = \frac{p'_{t,2,ideal}}{1 + \frac{p'_{t,1} - p_1}{p'_{t,1}} \cdot \Omega_{rot}} \tag{2}$$

$$h_{t,2} = h_{t,1} + I \cdot U_2^2 \tag{3}$$

$$\Omega_{rot} = \sum \omega_{rot} = \omega_{inc} + \omega_{dif} + \omega_{CH} + \omega_{sf} + \omega_{BL} + \omega_{HS} + \omega_{\lambda} + \omega_{mix} + \omega_{cl} + \omega_{cr} \tag{4}$$

$$I = I_{bl} + I_{df} + I_{leak} + I_{recir} \tag{5}$$

The total pressure loss coefficient of the impeller, Ω_{rot}, accounts for incidence losses, entrance diffusion losses, aerodynamic blockage, skin friction losses, blade and hub-to-shroud loading losses, abrupt expansion losses, mixing losses, pressure losses given by blade-to-blade pressure difference (in open impellers), clearance losses and super-critical Mach number losses. The work input coefficient I on the other hand includes loading losses, friction losses, leakage losses and recirculation losses.

The diffuser model is based on total enthalpy conservation (i.e., the diffuser is considered to be adiabatic) and pressure loss coefficients, following a similar approach to that of the impeller. In addition, the model considers flow deviation and blockage factors and is applicable to either vaned or vaneless diffuser designs (accounting for the vaneless space between impeller and diffuser). The vaneless diffuser is modelled through mass and angular momentum conservation (accounting for friction and diffusion losses) whilst the geometry of the vaned diffuser is defined by the area ratio, divergence angle and number of blades (varied in a predefined design space suggested by Aungier for preliminary design). In this work, vaneless diffusers are preferred in order to obtain a wider operating range, even though this implies a slightly lower rated (peak) efficiency; it is to note that this flexibility is essential for SmGTs [32].

A compressor map showing the effect of incorporating variable inlet guide vanes (VIGVs) is shown in Fig. 5. For each shaft speed, two lines are overlaid. The solid constant-speed lines correspond to a compressor without VIGVs while the dashed lines represent the same compressor with a row of VIGVs (whose stagger angle adapt to the corresponding operating conditions to yield maximum efficiency). For the compressor incorporating VIGVs, each constant-speed lines is comprised of three segments, corresponding to the different control strategies applied. Starting from compressor choke (rightmost operating point), the following sections are identified when mass flow rate is reduced.

- From compressor choke to peak efficiency, the constant speed line is virtually the same as for the compressor without VIGVs.
- In a second section, in blue, pressure ratio is slightly lower than if no VIGVs were incorporated. Mass flow rate is controlled through the positioning of VIGVs at different stagger angles in order to achieve peak impeller efficiency for each mass flow rate. This operating strategy is applied until the VIGVs are closed 50ºwith respect to the axial direction, at which angle the high incidence losses at the inlet to the VIGVs increase exponentially [29].

[1]The utilisation of VIGVs is not mandatory. This is a case-specific design choice for enhanced flexibility.

- In the third and last section, shown in red with cross markers, mass flow is reduced further but the position of VIGVs remains constant at 50º. This causes a quick drop in efficiency.

It is observed that the utilisation of VIGVs enables a wider operating map on the left, around to the surge line, which is instrumental to maximise the annual production of electricity/water (i.e., increased capacity factor).

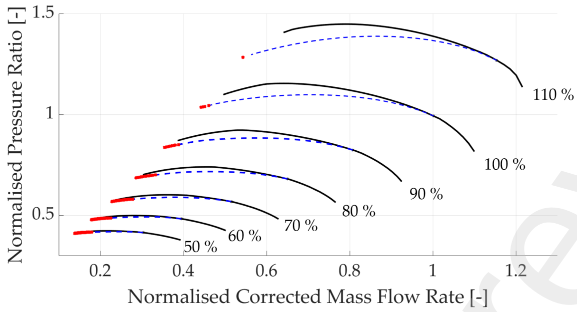

Figure 5: Combined normalised compressor performance map which shows the differences of using or not VIGVs at the impeller inlet.

3.1.2. Solar subsystem

The solar receiver is a cylindrical cavity with an hemispherical bottom cap whose geometry is presented in Fig. 6. This indirectly illuminated receiver has already been demonstrated in Europe [8] and it is one of the most widely considered receiver designs in parabolic dish Stirling systems [33], despite the potential occurrence of hot spots and also the potentially large temperature difference between receiver wall and working fluid, which may trigger mechanical issues as highlighted in literature [34].

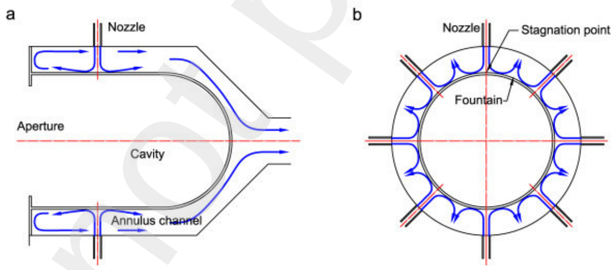

Figure 6: Axial (a) and radial (b) cross section schematics of the impinging solar receiver [35].

The solar dish is modelled under the assumption of a Gaussian distribution of the solar flux, corrected as proposed by Aichmayer *et al.* [36], and considering a focus/diameter ratio of about 0.6. This is the optimal shape of the parabola as demonstrated in the OMSoP Project [37], yielding the highest concentration ratio and highest temperatures.

The methodology adopted to design the receiver is based on the work by Wang [38]. It is an inverse design method [39] taking into consideration the following requirements: interaction with the impinging jet, minimum heat transfer coefficient (heat loss) and pressure drop. The main dimensions of the receiver are set following the recommendations provided by Wang *et al.* [40], considering three degrees of freedom: i) diameter of the cavity, D_{cav}, ii) nozzle diameter, d, and iii) total number of nozzles, n (see Fig. 6). The interaction between jets is negligible for high values of the ratio from the curvilinear distance between nozzle-centre and jet-centre to the diameter of the nozzle, but the undesired interference will increase as this ratio decreases. The first requirement yields the following equation:

$$P_{jet}/d = \pi \cdot j \cdot (D_{cav} + 2t)/(n \cdot d) \geq 8 \tag{6}$$

where P_{jet} stands for jet pitch, t is wall thickness, and j is the number of nozzle rows in the axial direction.

The local Nusselt number on the outer receiver wall decreases far from the axis of the impinging jet. Therefore, heat transfer ‘valleys’ are located between the stagnation areas (impingement of jet on receiver wall) and the ’fountain’ region (halfway between adjacent jets), whereas the maximum heat transfer coefficient is located in the ’fountain’ region between two impinging jets (see Fig. 6). In order to reach the targeted wall temperature, the heat transfer coefficient at the ’fountain’ regions (region between two impinging jets) must be higher than the required peak heat transfer coefficient $h_{req,max}$. This second requirement can be expressed as follows:

$$h_{mid} = \frac{0.156 \cdot k_{wf} \cdot \dot{m}^{0.75} \cdot Pr^{0.42} \cdot e^{-0.025 \cdot (\pi \cdot j \cdot (D_{cav}+2t)/(2n \cdot d))^2}}{(n \cdot \pi \cdot \rho \cdot \nu)^{0.75} \cdot d^{1.75}} \geq h_{req,max} \tag{7}$$

where ν is kinematic viscosity, $\dot{m}$ is mass flow rate, Pr is Prandtl number, ρ is air density and k_{wf} is thermal conductivity of the working fluid.

Finally, an upper bound of pressure losses is set to $\Delta P/P = 3\%$, in order to avoid a strong negative impact on turbine performance. Accordingly, the last requirement of the impinging receiver design can be expressed as follows, according to the discussion presented in [38]:

$$n \cdot d^2 \geq 4 \cdot \dot{m} / \left(\pi \cdot C_d \cdot \sqrt{0.06 \cdot \rho \cdot P}\right) \tag{8}$$

where C_d is the discharge coefficient of the nozzle, which depends on the configuration of the nozzle.

Two main differences between the receiver design code employed in the present paper and that developed in the reference work by Wang [38] are worth noting. First, while Wang’s code starts from a 2D axisymmetric model and then identifies the required distribution of heat transfer coefficients on the inner wall yielding optimum performance, the present code aims to achieve the smallest receiver design possible, always fulfilling the three aforelisted requirements. This general difference in the overall structure of the code has a minimum impact on the results obtained. Second, heat losses due to natural convection are accounted for in this work whereas they are neglected by Wang. To calculate these, the *Nusselt* number on the outer wall of the receiver is estimated with Eq.(9), taken from [41]. The approach adopted in this research is therefore deemed to provide a more conservative (safer) approach to receiver design than that used in the reference documents.

$$Nu = 0.0027 \cdot Gr^{0.54} \cdot \left(\frac{T_w}{T_\infty}\right)^{0.47} \cdot (2 + 1.8 \cdot \cos^3\theta)^{-3.62} \tag{9}$$

In Eq.(9), T_w and T_∞ are the temperatures of cavity wall and ambient air in Kelvin.

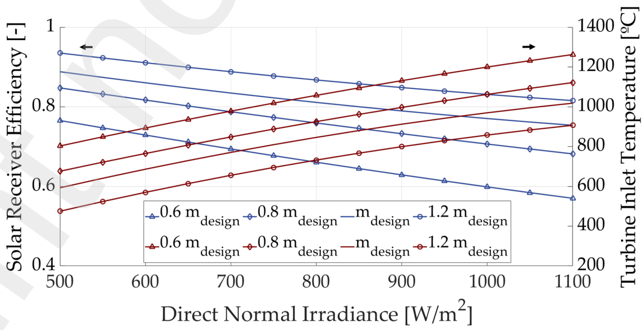

Figure 7: Impact of operating conditions on receiver performance.

The impact of operating temperature on receiver performance is shown in Fig. 7. It is observed that a lower irradiance on the collector yields lower operating temperatures (at set values of air mass flow rate), caused by both the lower thermal input and the lower thermal energy recovered on the high-pressure side of the recuperative heat exchanger. Moreover, as expected, a decrease of the operating temperature brings about higher receiver efficiencies thanks to reduced heat losses. Furthermore, the receiver tends to operate at higher efficiencies when the circulating mass flow rate is also higher, which suggests scaling up the receiver. Nevertheless, as highlighted by Gavagnin *et al.*

[4], this has a strong negative effect on the economics of the solar collector whose cost increases exponentially with size.

3.1.3. *Recuperator*

The recuperator is a critical component of a micro gas turbine given that it contributes some 30% of the total cost of the engine [42], and it cannot be considered a secondary element relative to turbomachinery. This sets the target to achieve as high recuperator efficiency as possible whilst, at the same time, ensuring small footprint, low cost and high reliability amongst other specifications [43].

Figure 8 shows estimates of effectiveness and specific weight of different types of recuperators gathered from literature [44, 45]. The specific weight of the recuperator matrix (excluding headers) is defined as the ratio of matrix weight to gas flow rate so, under the same effectiveness, the smaller the specific weight, the lighter and more compact the recuperator. This explains why primary surface heat exchangers (PSHEs) are the most common choice in microturbine applications [46].

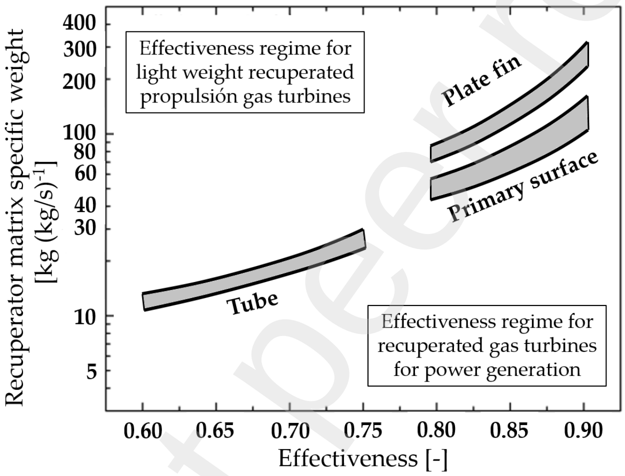

Figure 8: Comparisons of effectiveness and specific weight of the recuperator matrix (adapted from [44, 45])

The corresponding model employed to size (design) and model the performance of the recuperator is based on splitting the component into several (sub) heat exchangers of equal heat duty, *i*, following the methodology described by Nellis & Klein (2008) [47] to evaluate the overall conductance (UA). This calculation relies on the $\varepsilon - NTU$ approach presented in Eqs.(10-12).

$$\varepsilon = \frac{\dot{Q}_i}{\dot{C}_{min,i} \cdot (T_{H,i} - T_{C,i+1})} \qquad for \;\; i = 1...N \tag{10}$$

$$NTU_i = \frac{1}{1 - \dot{C}_i^*} \cdot log \frac{1 - \varepsilon_i \cdot \dot{C}_i^*}{1 - \varepsilon_i} \qquad for \;\; i = 1...N \tag{11}$$

$$UA_i = NTU_i \cdot \dot{C}_{min,i} \qquad for \;\; i = 1...N \tag{12}$$

Where N is the total number of (sub) heat exchangers, U is the global heat exchange coefficient and $\dot{C}_i^*$ the ratio of heat capacities $\frac{\dot{C}_{min,i}}{\dot{C}_{max,i}}$.

The off-design performance of the recuperator is modelled through the conductance ratio method, a methodology already presented and discussed in literature by some of the authors and other researchers [48–51]. Given the inlet conditions and mass flow rates at both sides of the recuperator, the outlet conditions can be calculated with Eqs. (13-15), where the rules to scale the rated value of conductance and to compensate for the variations of thermodynamic properties throughout the recuperator have been validated experimentally by the authors in [49], for fluids with both ideal and non-ideal gas behaviour.

$$\Delta P = \Delta P_{des} \cdot \frac{\dot{m}^2}{\dot{m}_{des}^2} \cdot \frac{\rho_{des}}{\rho} \tag{13}$$

$$\frac{1}{UA_{des}} = \frac{1}{hA_{hot,des}} + \frac{1}{hA_{cold,des}} \tag{14}$$

$$hA = hA_{des} \cdot \left(\frac{k}{k_{des}}\right) \cdot \left(\frac{\dot{m}\mu_{des}}{\dot{m}_{des}\mu}\right)^{0.8} \cdot \left(\frac{Pr}{Pr_{des}}\right)^{y} \tag{15}$$

Where $y = 0.3$ for the hot side and $y = 0.4$ for the cold side.

3.1.4. Turbine

The model of the radial-inflow turbine is based on the work by Aungier again [52] and it is therefore similar to that used for the compressor. This is seen in Fig. 9, presenting the indirect process used to design the machine as well as the most relevant design parameters: specifications and boundary conditions set by the thermodynamic cycle, specific speed, total-to-total velocity ratio, and other first-guess values used to initialise the calculation process. In contrast with the compressor model, there have been minor modifications with respect to the original model by Aungier and the loss correlations selected. A detailed discussion of the expander design model, complementary to the information presented in this work, can be found in [3].

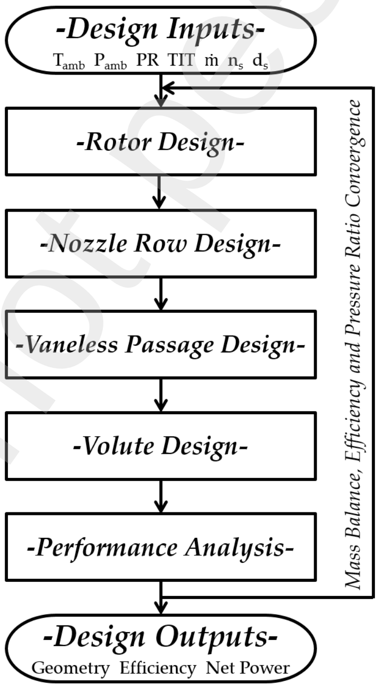

Figure 9: Turbine design flowchart.

Two constraints are used to size the rotor: i) the minimum hub radius compatible with the torque of the shaft and the materials used ($r_{out,shroud} < 0.9 \cdot r_{in}$), and ii) the lower limit of the axial length of the rotor ($\Delta z_r \geq 1.5 \cdot b_{in}$). Additionally, for mechanical integrity and to enable higher shaft speeds, the inlet flow at the design point is assumed to be radial ($\beta_{in} = 90$º) [3]. Considering profile losses, incidence losses, loss coefficients due to blade loading and hub-to-shroud loading effects, clearance losses and moisture losses (if any), the actual relative total pressure at the outlet is given by the rotor loss coefficient, Y_{rot}, as expressed in Eqs. (16 - 17).

$$Y_{rot} = \sum Y_{i,rot} = Y_p + Y_{inc} + Y_{BL} + Y_{HS} + Y_{cl} + Y_Q \tag{16}$$

$$p'_{t,out} = \frac{p'_{t,out,id} + Y_{rot} \cdot p_{out}}{1 + Y_{rot}} \tag{17}$$

In order to size the nozzle row, the normalised blade profile is calculated first. To this end, the vanes are geometrically set so as to match the required rotor inlet conditions and, then, the stagger angle yielding the required throat area is determined. At the same time, velocity distributions within the blade passage are checked to avoid inconsistencies and the nozzle throat area is fine tuned iteratively to avoid supersonic flow, often occurring at the outlet from the nozzles. The performance map of an exemplary radial-inflow turbine is presented in Fig. 10 showing normalised non-dimensional mass flow rate, pressure ratio and shaft speed.

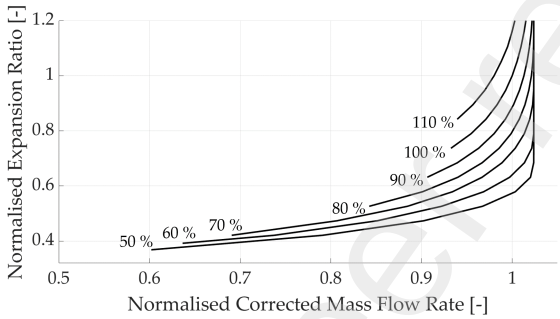

Figure 10: Normalised performance map of the turbine.

3.2. Reverse Osmosis

A schematic of the Reverse Osmosis unit is presented in Fig. 11, whose flow arrangement and equipment have already been described in a previous section. Three main unitary processes can be identified:

1. Pressurisation of feedwater from ambient pressure to operating pressure, compliant with the following requirement:

$$\Pi_{BD} - \Pi_P < p_F - p_P - \Delta p_{lossF-BD} \tag{18}$$

2. Solvent separation through the reverse osmosis membrane.
3. Pressure recovery from the outlet flow of concentrate.

It is further assumed that the outlet flows of freshwater and brine (p_p and $p_{BD,ERDout}$) are at atmospheric pressure, p_E.

The Specific Energy Consumption (SEC) of the process shown in Fig. 11 depends on the electric power consumption of the high-pressure and booster pumps (HPP and BP) and can be calculated through the corresponding flow rates, q_v, pressure, p, and pumps and engines efficiencies, η, as shown in Eq. (19):

$$SEC = \frac{\sum P_{W,HPP} + \sum P_{W,BP}}{q_{V,P}} = \frac{q_{V,HPP}}{q_{V,P}} \cdot \frac{p_{F,HPP} - p_F}{\eta_{HPP} \cdot \eta_{eng,HPP}} + \frac{q_{V,ERD}}{q_{V,P}} \cdot \frac{p_{F,HPP} - p_{F,ERDout}}{\eta_{BPP} \cdot \eta_{eng,BP}} \tag{19}$$

Then, the energy recovery process taking place in the isobaric chamber is characterised by Eqs. (20-21), whereas the ratio of volumetric flow rates through each stream is defined by Eqs. (22-24):

$$\eta_{ICH} = \frac{q_{V,ERD} \cdot p_{F,ERDout} + q_{V,BD} \cdot p_{BD,ERDout}}{q_{V,ERD} \cdot p_{F,ERDin} + q_{V,BD} \cdot p_{BD,ERDin}} \tag{20}$$

$$\varepsilon_{ICH} = \frac{p_{BD,ERDout} - \eta_{ICH} \cdot p_{BD,ERDin}}{\eta_{ICH} \cdot p_{F,ERDin} - p_{F,ERDout}} \tag{21}$$

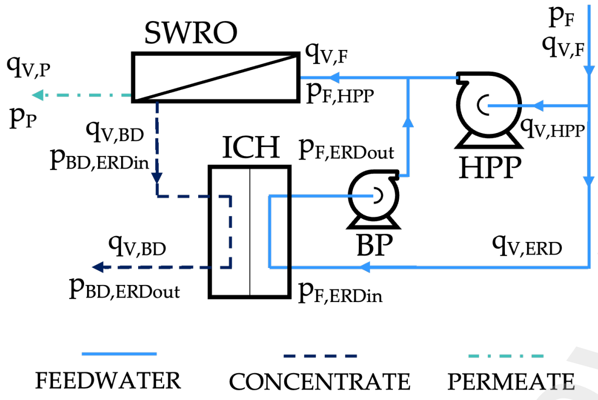

Figure 11: Schematic of Reverse Osmosis system, including an Energy Recovery Device (ERD).

$$q_{V,ERD} = q_{V,BD} \cdot \varepsilon_{ICH} \tag{22}$$

$$\frac{q_{V,ERD}}{q_{V,P}} = \left(\frac{1}{r_V} - 1\right) \cdot \varepsilon_{ICH} \tag{23}$$

$$\frac{q_{V,HPP}}{q_{V,P}} = \frac{1}{r_V} - \left(\frac{1}{r_V} - 1\right) \cdot \varepsilon_{ICH} \tag{24}$$

In this set of equations, r_v is the recovery rate of the process, defined as the ratio from permeate flow rate, $q_{V,P}$, to feedwater flow rate, $q_{V,F}$.

Figure 12 depicts an exemplary off-design performance representative of a seawater RO system working in Atlantic conditions, with water temperature of 22ºC. The operating pressure is set to 60 bar throughout the whole operating range, what enables increasing recovery rates in partial load operation. The main specific energy consumption remains at around 2 kWh/m^3 in all cases.

To assess the performance of the SWRO unit, the aforementioned model has been compared against the estimates provided by the software *Q*+ developed by LG Chem [26], widely used by the industry, and considering a single pressure vessel with seven LGSW440GR membrane modules [53]. It is to note that this membrane type has been selected for its ability to operate with higher rejection rates, what implies that a more reliable operation within a wide range of power input to the SWRO unit can be achieved in all climate conditions, thus adapting to the variable electric power produced by the SmGT unit.

Regarding sensitivity to boundary conditions, it is worth noting that both specific energy consumption and operating pressure increase with the salinity of seawater whereas the operation with higher feedwater temperatures reduces the power input range enabling an adequate quality of the permeate.

3.3. Zero Liquid Discharge

3.3.1. Experimental proof of concept of the ZLD system

Within the SOMIDEFF project, a proof-of-concept Zero-Liquid-Discharge system has also been developed. The concept is simple and relies on bubbling the hot exhaust gases from the SmGT into a well of brine through a specific diffuser design, as shown in Fig. 13. Operation of this system has been demonstrated, integrated into a Cussons P9001 micro gas turbine engine (3 kWe) installed in the Laboratory of Heat Engines at University of Seville.

A fast-acting pneumatic valve is used divert the host gases from the turbine exhaust to either the ZLD unit or the stack. The brine well and injection pipe are sized to minimise back pressure on the turbine, as this has a negative impact on the efficiency of the SmGT. The same applies to the diffuser, whose design stems from a compromise between the need to minimise back pressure whilst maximising the direct contact between gas and brine.

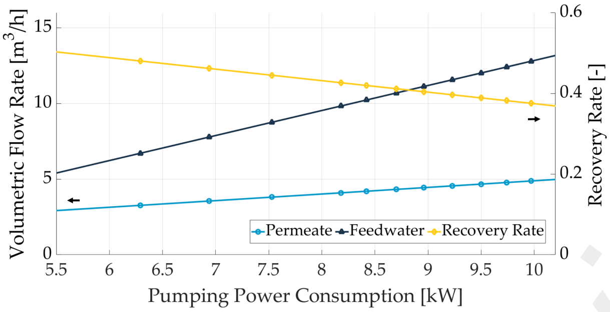

Figure 12: Off-design performance of the SWRO unit.

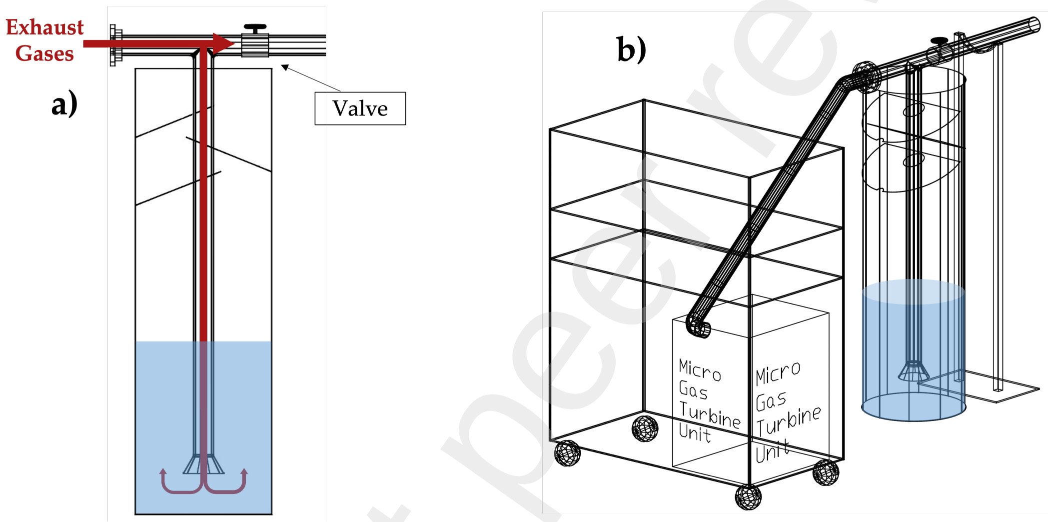

Figure 13: Configuration of the low-cost ZLD prototype. a) Cross-sectional view of the ZLD unit. b) Schematic showing global arrangement.

The thermal energy carried by the gas stream is used to evaporate water in the brine, and this increases the concentration of salt in the well. At full load (hence peak mass flow rate of gases into the well), water drift becomes a concern. Hence, in order to minimise this, baffles are installed inside the well above the brine level: droplets carried over by the gaseous stream impinge on the baffles, returning to the well for evaporation.

The performance of the prototype has been assessed for operation in batches and is illustrated in Fig. 14. Temperature measurements, logged with infrared imagery and thermocouples, indicate that the temperature of exhaust gases flowing across the ZLD drops from ~450ºC to ~70ºC. A picture of the ZLD in operation without the upper seal is also shown in Fig. 14, revealing the plume coming out from the well (high steam content), alongside a picture of the resulting solid waste (solid salt).

3.3.2. Performance modelling of the ZLD system

As already discussed in earlier sections of the paper, Zero-Liquid-Discharge concepts have recently gained importance, out of the growing desalination capacity worldwide and of the associated concerns about the impact that this highly-concentrated effluents have on the environment. The term brine is typically used to define the resulting by-product (waste) of desalination systems, whose salt concentration typically exceeds 55 mg/L [54]. Based on different technologies, ZLD systems tackle this problem by trying to increase the concentration of the brine further with the ideal objective to completely remove the water content of it; accordingly, the resulting waste would be in solid state and would therefore represent a much more manageable product, easier to store and transport and with a lower potential to harm the environment. For these reasons, ZLD systems are increasingly being seen as mandatory requirements

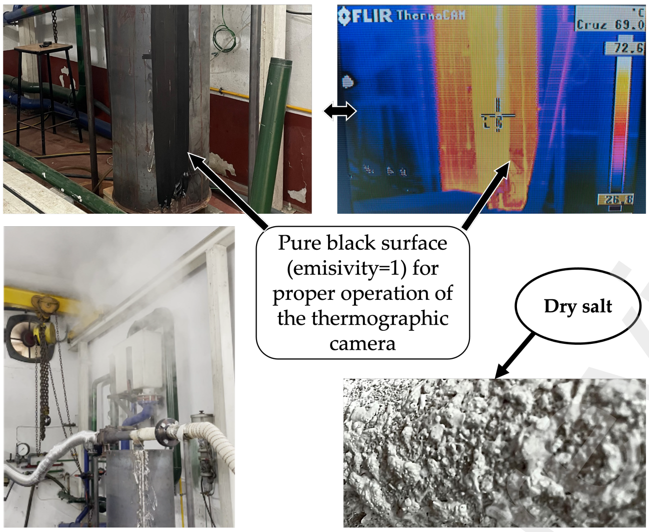

Figure 14: Graphical information of the proof-of-concept ZLD.

in some industrial processes [55].

Indeed, reducing the amount of energy needed to minimise the discharge of liquid, highly-saline effluents is behind the growing interest in coupling membrane-based RO technology with ZLD systems, given the energy-intensive nature of this process [56]. In this regard, it is also to note that RO cannot be used for the further concentration of effluents given that these membranes can work with feedwaters whose salinity is not higher than 80 g/L, in order to avoid membrane fouling and scaling. For brines with higher concentrations, a phase-change ZLD system is needed [57–59].

In the actual SOLMIDEFF system, the ZLD unit works very similarly to the proof-of-concept unit tested at the lab (Fig. 14): the concentrate resulting from the RO process is fed into an evaporation chamber, which is nothing but a direct contact heat exchanger where the thermal energy of the exhaust gases from the SmGT (at 225-325ºC) is used to evaporate water in the brine (therefore raising the concentration of this stream). Moreover, in order to enhance the performance of the ZLD unit, the brine flowing into the evaporation chamber is preheated in another chamber fed by the stack gases at a lower temperature of ~60-100ºC (given that a large portion of their sensible heat has already been harvested in the evaporation process). This is shown schematically in Fig. 15.

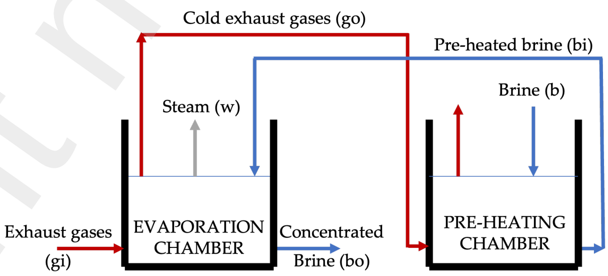

Figure 15: Conceptual representation of the Zero Liquid Discharge unit.

The ZLD system is modelled through the methodology already presented and discussed by some of the authors in [16]. The ratios of mass flow m_{bo}/m_{bi} and salinity S_{bo}/S_{bi} are estimated for operating conditions different to the rated values, noting that there is an operational limit of the inlet mass flow ratio (m_{gi}/m_{bi}). In particular, the mass flow rate of exhaust gases from the turbine must be, at least, 10 times higher than the mass flow rate of brine inasmuch as, otherwise, the stability and sustainability of the evaporation process would be compromised [60].

Figures 16(a) and 16(c) show trends of the ratio from inlet to outlet salinity ratio of the brine (S_{bi} / S_{bo}), for values of inlet brine salinity of S_{bi} = 0.07 kg/kg and S_{bi} = 0.12 kg/kg respectively. This ratio increases for higher temperatures of either the exhaust gases from the turbine (T_{gi}) or the inlet brine (T_{bi}) until saturation is reached, thus setting the limit up to which brine could be concentrated. Pre-heating the brine to the lowest temperature (T_{bi} = 60ºC) enables to reach the saturation point if the inlet temperature of the exhaust gases inlet temperature (T_{gi}) is 305ºC, and this latter temperature decreases to no more than 290ºC when the brine is pre-heated to 100ºC. The inlet to outlet mass flow rates of the brine (m_{bi} / m_{bo}) is shown on the right charts, Figs. 16(b) and 16(d). As either temperature increases (brine or gases), more water is evaporated and salinity becomes higher. Moreover, linking all charts, it is also observed that the mass flow ratio lines for different brine temperatures and concentrations change curvature and tend to collapse into a single line which corresponds with saturated brine conditions. This is an interesting result though it must be acknowledged that curves past saturation point are merely hypothetical.

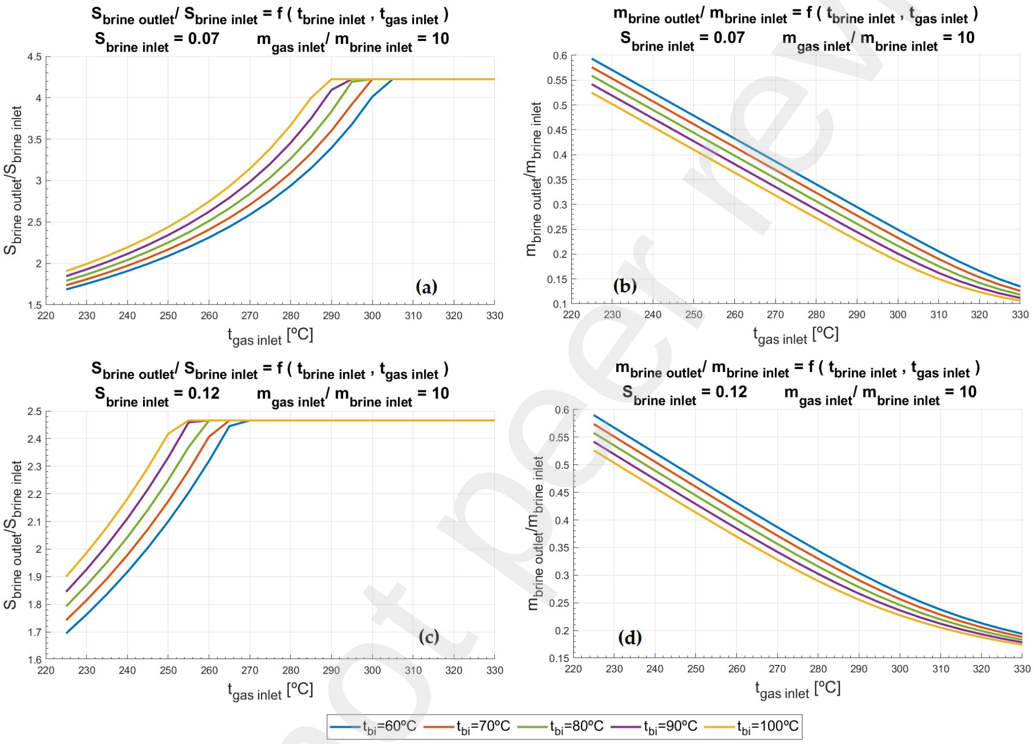

Figure 16: **(a)** Ratio between outlet and inlet brine salinities as a function of temperatures of inlet brine and inlet exhaust gases from the turbine in evaporation chamber, for S_{bi}=0.07 kg/kg and m_g/m_b=10; **(b)** Ratio between outlet an inlet brine mass flow rates as a function of temperatures of inlet brine and inlet exhaust gases from the turbine in evaporation chamber, for S_{bi}=0.07 kg/kg and m_g/m_b=10; **(c)** Ratio between outlet and inlet brine salinities as a function of temperatures of inlet brine and inlet exhaust gases from the turbine in evaporation chamber, for S_{bi}=0.12 kg/kg and m_g/m_b=10; **(d)** Ratio between outlet an inlet brine mass flow rates as a function of temperatures of inlet brine and inlet exhaust gases from the turbine in evaporation chamber, for S_{bi}=0.12 kg/kg and m_g/m_b=10 [16]

4. Validation

Given the lack of available SmGT experimental data in literature, it is not possible to validate the system presented in this work directly. Nevertheless, the accuracy of the model developed for each component of the system can be verified individually, either theoretically or experimentally, in order to ensure that the results obteined are trustful:

- **Turbomachinery**: the modelling approach of compressor and turbine are widely known in literature and have been validated extensively against a considerable set of experimental data [27, 52], in addition to being used in past works by the authors [5].
- **Solar subsystem**: the solar dish has been modelled according to the work carried out by Aichmayer *et al.* for the OMSoP project [36], whereas the methodology applied to model the impinging solar receiver follows

the inverse design method proposed by Wang [39]. Both models were validated through experimentally at the Royal Institute of Technology in Stockholm (KTH) [38].

- **Recuperator**: the recuperator is modelled following the well known method described by Nellis & Klein (2008) [47], whilst the conductance ratio method used to estimate the off-design performance of the recuperator was previously validated experimentally by the authors [49].
- **Reverse Osmosis**: the validation of the design and off-design models of performance of the RO system is supported on the software Q+ [26], whose accuracy is widely acknowledged within the industrial and scientific communities.
- **Zero Liquid Discharge**: the reduction of the water content of the concentrate in the ZLD unit has been verified in the previous section, although further experimental validation for continuous operation is needed.

5. Results

The description provided so far in this paper depicts a tightly integrated system with a larger potential for overall energy utilisation than water desalination systems based on solar photovoltaic or wind power. Nevertheless, in order to verify and quantify this, it is mandatory to assess the performance of the system. This is presented now.

The general boundary conditions considered in this assessment correspond to the Canary Islands, given their need for freshwater and high availability of solar energy; the applicability to neighbouring coastal locations in Northern Africa is an additional feature making this location interesting and representative of a larger area. In particular, ambient conditions have been generated with METEONORM v.7 [61], gathering records form the last 25 years and establishing 95 percentile values, whereas seawater composition and temperature have been collected from the guidebook by Wilf and Awerbuch [62]:

- Ambient temperature: 26.4 ºC.
- Direct Normal Irradiance: 796 W/m^2.
- Water temperature: 22.0 ºC.
- Total Dissolved Solids (TDS) of feedwater: 38739 ppm.

5.1. Rated Performance

The specifications of major equipment are set to the values listed in Table 2 for a preliminary assessment, according to the discussions presented in foregoing sections of the paper.

The application of the design and performance models shown in earlier sections of the paper to the specifications in Table 2 yields the performance summarised in Table 3 for a system with the layout shown in Fig. 2. The net efficiency of the SmGT is around 26%, a value that is in line with the performance reported by the main Original Equipment Manufacturers of this type of engines [63]. The rated electric power is set to 10 kWe, which is mostly consumed by the pumps in the RO module -producing 4.68 m^3/h of fresh water-; the remaining power is consumed by the auxiliary systems needed.

Parameter	Units	Value
Solar Energy Collection		*Calculated*
Dish aperture area	[m^2]	65.87
Solar energy input	[kWt]	52.44
Collector efficiency	[%]	89.87
Receiver efficiency	[%]	81.87
Gas Turbine		
		Calculated
Isentropic compressor efficiency	[%]	78.77
Isentropic turbine efficiency	[%]	81.58
Receiver pressure drop	[%]	1.37
		Set
Recuperator effectiveness	[%]	85.0
Mechanical efficiency	[%]	98.0
Generator efficiency	[%]	98.0
Combustor pressure drop	[%]	2.0
Recuperator hot pressure drop	[%]	2.5
Recuperator cold pressure drop	[%]	2.5
Air filter pressure drop	[%]	2.0
Reverse Osmosis		*Set*
Isobaric chamber (ERD) efficiency	[%]	97.0
High pressure pump efficiency	[%]	87.0
Booster pump efficiency	[%]	80.0

Table 2: Specifications of major equipment in SOLMIDEFF.

Table 4 presents the heat and mass balance of the overall SOLMIDEFF system, supporting the results in 3. Streams 1 to 9 correspond to the SmGT whereas the water treatment subsystem is defined by streams 10 to 21.

Parameter	Units	Value
Micro Gas Turbine		
Power output	[kWe]	10.0
net efficiency	[%]	26,04
Solar-electric efficiency	[%]	19.15
Air mass flow rate	[kg/s]	0.121
Pressure ratio	[-]	3.5
Turbine inlet temperature	[K]	1123.1
Exhaust temperature	[K]	531.1
Shaft speed	[rpm]	134,294
Reverse Osmosis		
Freshwater production	[m^3/h]	4.68
Recovery rate	[%]	38.7
Operating pressure	[bar]	59.6
Specific Energy Consumption	[kWh/m^3]	2.03
TDS of concentrate	[ppm]	59,500
Pumping power	[kWe]	9.5
Membrane area	[m^2]	286
Zero Liquid Discharge		
Mass flow rate	[kg/s]	0.011
Salinity of outflow	[kg/kg]	0.286

Table 3: Performance of SOLMIDEFF. Component specifications are reported in Table 2

Micro Gas Turbine			
Stream	p [bar]	T [K]	h [kJ/kg]
1	1.013	299.5	425.84
2	0.993	299.5	425.85
3	3.464	461.9	590.09
4	3.377	842.9	995.90
5	3.331	1123	1314.6
6	3.264	1123	1314.5
7	1.071	907.1	1067.3
8	1.045	531.1	661.52
9	1.013	531.1	661.52
Sea Water Reverse Osmosis			
Stream	p [bar]	$\dot{m}$ [m^3/h]	TDS [ppm]
10	1.621	12.1	38,739
11	1.621	4.77	38,739
12	59.60	4.77	38,739
13	1.621	7.33	38,739
14	57.75	7.33	38,739
15	59.60	7.33	38,739
16	59.60	12.1	38,739
17	1.013	4.68	116.52
18	58.45	7.42	62,564
19	1.013	7.42	62,564
20	1.013	7.42	62,564
21	1.013	-	62,564

Table 4: Heat and mass balance of the reference case for the SOLMIDEFF system without ZLD operation.

The recovery rate of the RO module in SOLMIDEFF at design conditions is 39%, although this value increases as pump consumption decreases, sustaining the maximum pressure as described in the previous section. This recovery rate is equivalent to a Specific Energy Consumption of 2.03 kWh/m^3, accounting for the RO module only (i.e., excluding any water steam produced by the ZLD unit), which translates into a Solar Specific Energy Consumption of 10.6 kWh/m^3 when the efficiency of the topping SmGT system is accounted for.

The ambient temperature play an important role in the turbomachinery design process since the air density is significantly dependent on the temperature. A different ambient temperature supposes that, for the same mass flow rate, a higher volumetric flow rate must go through the SmGT, and of course a higher sizing of turbomachinery must be considered. Besides, the pressure ratio which maximised the net efficiency of the simple recuperated open cycle also rely on the ambient temperature, introducing a twofold influence on the SmGT. Table 5 lists some of the parameters that are influenced by ambient temperature.

Parameter	**Units**	**Value**	
Ambient temperature	**[K]**	**293**	**313**
Compressor & Turbine			
Mass Flow Rate	$[kg/s]$	0.120	0.141
Pressure Ratio	[-]	3.5	3.3
Shaft Speed	[rpm]	135,594	121,722
Compressor			
Total-to-Total Efficiency	[%]	78.75	78.34
Rotor Inlet Hub Radius	[mm]	2.20	2.40
Rotor Inlet Shroud Radius	[mm]	17.6	19.8
Rotor Outlet Radius	[mm]	35.7	39.9
Turbine			
Total-to-Total Efficiency	[%]	80.73	81.28
Rotor Inlet Radius	[mm]	36.8	36.7
Rotor Outlet Shroud Radius	[mm]	25.9	27.1
Rotor Outlet Hub Radius	[mm]	3.0	3.1

Table 5: Sensitivity analysis of the sMGT turbomachinery design against ambient temperature

5.2. *Off Design Performance*

This section is aimed at presenting the sizing process of the SOLMIDEFF system according to the environmental conditions of the site (Direct Normal Irradiance and ambient temperature) and, also, to assess how a particular system performs under different daily conditions in Gran Canaria (Canary Islands); to this latter end, an example of days with clear and hazy skies are considered. As a summary of some of these aspects, the performance map of this sizing process for every combination of DNI and ambient temperature is presented.

Compressor-turbine matching in the solar micro gas turbine is adapted from Razak for a simple, open-cycle industrial gas turbine [24], incorporating the effect of pressure drops introduced by the recuperative heat exchanger. The iterative process in the cited reference is nevertheless modified in order to have it controlled by the required turbine inlet temperature TIT and direct normal irradiance DNI, rather than shaft speed power output setting. Furthermore, for simplicity, inlet and exhaust losses are neglected ($P_{intake} = P_{exhaust}$) and the gas constant R and isentropic index γ are determined under the assumption of dry air. A graphical summary of changes from the original method is shown in Fig. 17.

Engine operation relies on three main control strategies, aimed at preventing overheating and/or overspeeding of the engine under very high insolation. In particular, when direct normal irradiance DNI increase:

- Shaft speed of turbomachinery can be increased, yielding higher throughput and pressure ratio. This yields lower turbine outlet temperature, therefore reducing the recuperative potential of the engine (i.e., lower temperature at receiver inlet). The cumulative effect of a higher mass flow rate and lower temperature at receiver inlet increases the amount of concentrated solar energy absorbed for the same turbine inlet temperature.
- If this is not enough to manage the large solar input, turbine inlet temperature is allowed to rise to 25ºC higher than the design value. This strategy can nevertheless not be used for long periods of time (given the severe reduction of the useful life of the turbine).
- Lastly, in case of continued operation under this undesired conditions (lower than 1% yearly as estimated by the METEONORM database [61]), the solar concentrator would have to be defocused. This is, unfortunately, not practical given that defocusing the concentrator implies increasing the spillage at the receiver window, thus

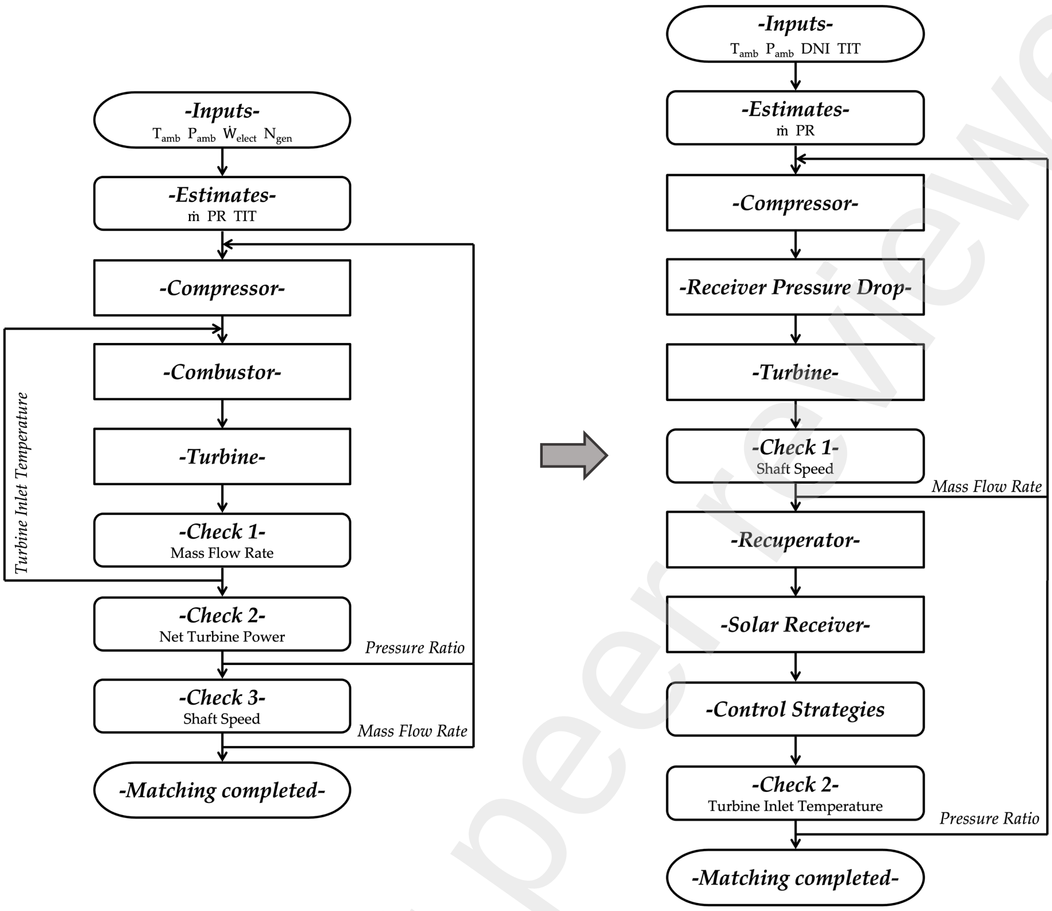

Figure 17: Comparison of the reference compressor-turbine matching process in [24] (a) and the process followed in this work (b)

compromising the mechanical integrity of this component. In other words, if defocusing were needed, the system would have to be shut down.

On the other end of the operating range, reducing the heat input to the system implies either of the following alternatives: turbine inlet temperature is reduced for somewhat constant mass flow rate, or mass flow rate is reduced whilst keeping turbine inlet temperature at the rated value. In either case, the pressure ratio of the engine is reduced, hence lifting turbine exhaust temperature for constant turbine inlet temperature, and this poses the risk to overheat the recuperator. Therefore, a limit on turbine exhaust temperature is set to 650ºC, assuming that the recuperator is manufactured from Stainless Steel without specific treatments (e.g. ceramic coatings) [46]. The impact of this constraint on part-load efficiency is illustrated in Fig. 18.

As discussed previously, the presence of VIGVs helps enhance the performance of the machine for operating conditions closer to the surge line, but the running line of a standard engine without Variable Nozzle Guide Vanes (VNGVs) is far from this region of the compressor map. Indeed, at reduced loads, even if mass flow rate and/or turbine inlet temperature are reduced, so is pressure ratio, hence moving the operating conditions to lower regions of the map where the presence of VIGVs is not providing any added flexibility. Based on this, the utilisation of variable compressor geometry (i.e., VIGV) comes together with the adoption of variable nozzle guide vanes in the expander (VNGV). This combination is required to avoid derating the part-load performance of the engine through the adoption of a lower turbine inlet temperature once the inlet temperature to low-pressure side of the recuperator (turbine exhaust temperature) achieves the maximum value allowed by materials. In particular, the incorporation of Variable Nozzle Guide Vanes in the expander enables reducing the inlet are to the nozzles at part load, thus keeping pressure ratio at or close to the rated value. This higher pressure ratio than in the standard engine (without VNGVs) also yields a larger

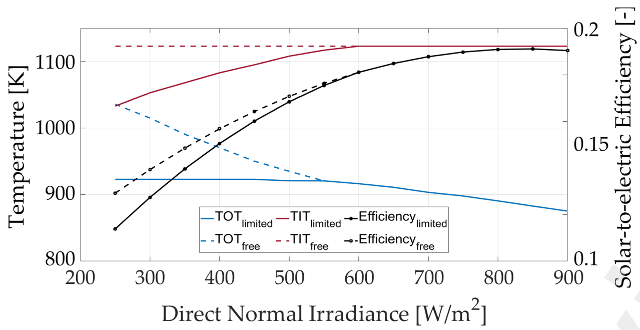

Figure 18: Part-load efficiency for a system with recuperator temperature limited to 650ºC.

temperature drop across the turbine, thus enabling operation at low partial loads without the need to reduce turbine inlet temperature. This has a twofold beneficial effect. From a system standpoint, it means higher part-load efficiency due to the higher pressure ratio and turbine inlet temperature. For the compressor, it means higher pressure ratios at low mass flow rates, thus moving the running line closer to surge and to the higher efficiency region of the compressor map. Accordingly, the utilisation of VIGVs in the compressor, whose impact on compressor inlet flow was described in the previous section, is instrumental to enable such operation.

The strong influence of incorporating VNGVs on system performance is better understood by observing the running lines of compressor and turbine on their respective performance maps when VNGVs are or are not used. Figure 19 shows this information for a representative solar micro gas turbine where DNI ranges from 250 W/m^2 to 900 W/m^2 at constant ambient temperature (26.4ºC). The blue and red solid lines correspond to compressor and turbine with any variable geometry feature, whilst the blue and red dotted lines are those of the compressor and turbine incorporating VIGVs and VNGVs respectively; the low mass flow end of these latter running lines are set by the minimum TIT drop compliant with a surge margin of at least 10% (note that mass flow rate is reported in corrected values to account for the effect of inlet pressure and temperature). For the sake of clarity, turbine maps for three different VNGVs angles only are shown in Fig. 19: design point (fully open), 75% closed and 55% closed.

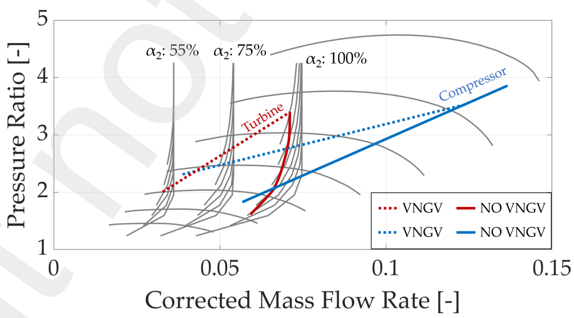

Figure 19: Running lines of the SmGT. Blue and red lines correspond to compressor and turbine. Solid and dotted correspond to machines with fixed geometry and machines with variable geometry (VIGVs for compressor and VGNVs for turbines) respectively.

The global impact of variable geometry on system performance is shown on Fig. 20, showing the pressure ratio and efficiency (solar-to-electric efficiency) of solar micro gas turbines with and without variable geometry across the entire load range, for the same rated output and efficiency. Two main features are observed. First of all, the superior performance (efficiency) of the solar micro gas turbine incorporating variable geometry compressor and turbine is shown. Indeed, despite having the same rated efficiency, the part-load efficiency curve of the variable geometry SMGT is much more resistant to load reductions thanks to the higher pressure ratio (and turbine inlet temperature). Second, the wider operating range without having to shut the engine down is also visible. This confirms the interest of adopting variable geometry turbomachinery in spite of the higher cost anc complexity.

The impact of the different performance, illustrated in Fig. 20, on the production of electricity of the SMGT for

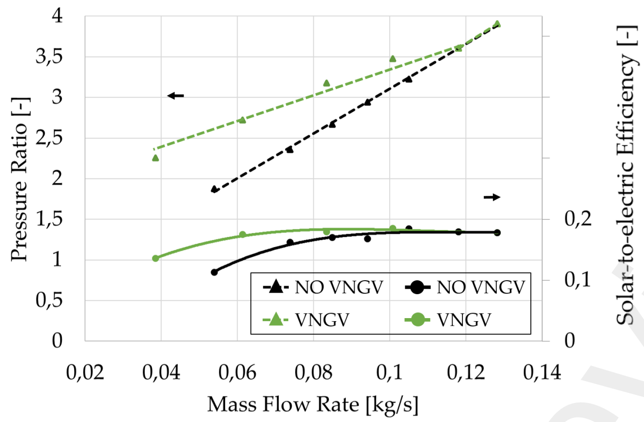

Figure 20: Part-load performance of solar micro gas turbines with (black) and without (green) variable geometry turbomachinery. Pressure ratio (dashed) and solar-to-electric efficiency (solid) curves are shown.

two different sets of boundary conditions -sunny and cloudy days- is summarised in Figs. 21 and 22 and in Tables 6 and 7. Both of these tables provide detailed information about the performance of the operating parameters of the standard engine without variable geometry and those of the system incorporating variable geometry. The benefits of a stronger resistance of pressure ratio and turbine inlet temperature of the variable geometry engine when load is reduced (i.e., higher pressure ratio and turbine inlet temperature) translate into higher efficiency and, therefore, production of electricity. As expected, this is more visible in the case of a cloudy day.

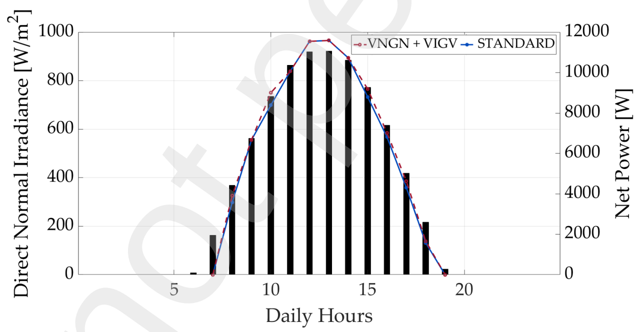

Figure 21: Net power production of the SmGT during a sunny day

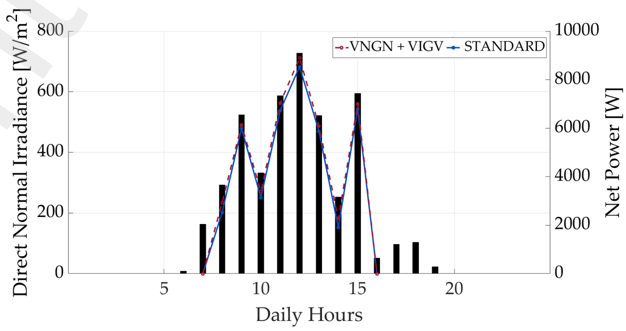

Figure 22: Net power production of the SmGT during a cloudy day

Hour	T_{amb}	η_{comp}[%]		η_{turb}[%]		$\eta_{sol-elec}$[%]		Pressure Ratio [-]		TIT [K]	
		VIGV VNGV	Standard	VIGV VNGV	Standard	VIGV VNGV	Standard	VIGV VNGV	Standard	VIGV VNGV	Standard
8:00	28.7ºC	72.93	78.72	86.26	81.41	16.09	14.74	2.68	2.25	1,103	1,053
9:00	29.9ºC	75.82	79.54	83.58	81.77	18.01	17.99	3.31	2.82	1,123	1,098
10:00	31.0ºC	78.15	78.59	81.62	79.65	18.59	17.32	3.60	3.45	1,123	1,108
11:00	32.1ºC	77.71	77.71	81.05	81.05	17.68	17.68	3.85	3.85	1,113	1,113
12:00	32.9ºC	77.07	77.07	83.25	83.25	19.07	19.07	4.14	4.14	1,138	1,138
13:00	33.6ºC	77.04	77.04	83.23	83.23	19.08	19.08	4.13	4.13	1,143	1,143
14:00	34.1ºC	77.14	77.14	83.62	83.62	18.40	18.40	4.10	4.10	1,113	1,113
15:00	33.2ºC	78.20	78.16	81.16	80.33	18.04	17.27	3.61	3.57	1,123	1,108
16:00	33.2ºC	76.43	78.87	82.14	79.61	17.30	16.77	3.42	3.05	1,123	1,103
17:00	33.2ºC	76.73	78.55	84.26	81.79	16.75	15.58	2.70	2.41	1,098	1,068
18:00	33.7ºC	73.50	75.02	86.60	83.78	11.58	11.00	2.01	2.01	1,038	1,013

Table 6: Variation of key performance parameters of engines with and without variable geometry, in a sunny day

Hour	T_{amb}	η_{comp}[%]		η_{turb}[%]		$\eta_{sol-elec}$[%]		Pressure Ratio [-]		TIT [K]	
		VIGV VNGV	Standard	VIGV VNGV	Standard	VIGV VNGV	Standard	VIGV VNGV	Standard	VIGV VNGV	Standard
8:00	21.2ºC	72.36	79.12	87.10	80.67	15.18	13.09	2.45	2.01	1,073	1,028
9:00	22.2ºC	72.92	78.55	85.00	80.32	17.79	17.36	3.25	2.72	1,123	1,093
10:00	23.2ºC	72.43	79.28	86.43	81.21	15.52	14.35	2.52	2.13	1,083	1,043
11:00	24.3ºC	75.52	78.32	83.41	79.89	18.20	17.41	3.43	2.93	1,113	1,103
12:00	25.5ºC	78.11	78.73	80.79	79.28	18.57	17.82	3.56	3.42	1,123	1,108
13:00	26.0ºC	74.02	78.58	85.01	80.45	17.70	17.07	3.29	2.72	1,108	1,093
14:00	26.1ºC	72.58	78.61	87.05	81.33	13.61	11.43	2.24	1.88	1,063	1,018
15:00	26.3ºC	75.02	78.58	83.43	79.80	17.85	17.33	3.45	2.96	1,118	1,103

Table 7: Variation of key performance parameters of engines with and without variable geometry, in a partly cloudy day

6. CONCLUSIONS

A novel solar desalination system driven by a SmGT for off-grid applications is assessed in this work, with a specific focus on the modelling of each subsystem. A complete set of deatiled models enables characterising the design and off-design performance of the SOLMIDEFF system, which is comprised of the following components: i) a solar-to-electric power conversion unit based on dish-mGT, ii) a RO unit for desalination or industrial water treatment and iii) a ZLD system for the treatment of desalination or industrial process effluents. The computational tool enables to size the components and to evaluate their off-design performance for different design configurations, including the incorporation of VIGV in the compressor.

The following relevant conclusions are drawn:

- Incorporating variable inlet guide vanes in the compressor has the effect of extending the operating range of the engine, enabling operation at low mass flow rates and high pressure ratios (close to the surge). Since using VNGVs in the turbine enables operation at high pressure ratio even when mass flow rate is reduced at part load, their combination with VIGVs (Variable Inlet Guide Vanes) at compressor inlet is crucial to increase the off-design performance of the SmGT proposed in this work.
- Incorporating VIGVs in the compressor without considering a radial turbine with VNGVs (Variable Nozzle Guide Vanes) seems to be of no interest, since the running line of the compressor does not approach the surge line.
- Since recuperators made of stainless steel cannot operate at temperatures higher than 650ºC, operation at part-load using standard (constant geometry) SmGT implies that turbine inlet temperature be decreased what, in turn,

reduces turbine outlet temperature. This, unfortunately, brings about a faster efficiency decay when running the system in partial load.
- The ZLD system is capable of saturating the concentrate of the RO unit, enabling zero liquid discharge. This has been proved experimentally for operation in batches, where the concentrate has been reduced to solid (dry) salts.
- If higher flexibility at partial load is needed by a RO system, a moderate recovery rate at rated conditions is recommended.

Globally, the system presented in this work shows interesting features, mostly a very high flexibility, robustness and easy integration with backup fuels of different types. These are all promising characteristics for applications where a robust and reliable polygeneration system (power, heat and fresh water) is needed, able to ensure the security of supply of these primary services for off-grid communities.

Future work by the authors will include the analysis of transient operation (currently supported by a research project funded by the Regional Council for Research of the Government of Andalusia, Spain), due to the dissimilar characteristics of the solar gas turbine and reverse osmosis in this regard, as well as an economic assessment in different latitudes. This is a fundamental step towards assessing the commercial feasibility of the system proposed.

Acknowledgement

This manuscript has been developed in the framework of SOLMIDEFF project, under grant agreement RTI2018-102196-B-100, funded by MCIN/AEI/10.13039/501100011033 and by "ERDF A way of making Europe". This manuscript was also partially developed within the MONSIEUR project, under grant agreement P20_01102, funded by Junta de Andalucía and the European Regional Development Fund.

References

[1] The global economy, https://www.theglobaleconomy.com/rankings/, accessed: 2020-10-26.

[2] The world bank, https://data.worldbank.org/indicator/EG.USE.ELEC.KH.PC, accessed: 2021-10-26.

[3] G. Gavagnin, Techno-economic optimization of a solar thermal power generator based on parabolic dish collector and micro gas turbine, Ph.D. thesis, University of Seville (2019).

[4] G. Gavagnin, D. Sánchez, G. S. Martínez, J. M. Rodríguez, A. Muñoz, Cost analysis of solar thermal power generators based on parabolic dish and micro gas turbine: Manufacturing, transportation and installation, Applied Energy 194 (2017) 108–122. doi:https://doi.org/10.1016/j.apenergy.2017.02.052.

[5] G. Gavagnin, S. Rech, D. Sánchez, A. Lazzaretto, Optimum design and performance of a solar dish microturbine using tailored component characteristics, Applied Energy 231 (2018) 660–676. doi:https://doi.org/10.1016/j.apenergy.2018.09.140.

[6] G. Gavagnin, D. Sánchez, J. M. Rodríguez, A. Muñoz, G. S. Martínez, Economic-competitiveness of dish-mgt solar power generators, in: Turbo Expo: Power for Land, Sea, and Air, Vol. 50831, American Society of Mechanical Engineers, 2017. doi:https://doi.org/10.1115/GT2017-64351.

[7] D. Sánchez, A. Bortkiewicz, J. M. Rodríguez, G. S. Martínez, G. Gavagnin, T. Sánchez, A methodology to identify potential markets for small-scale solar thermal power generators, Applied Energy 169 (2016) 287–300. doi:https://doi.org/10.1016/j.apenergy.2016.01.114.

[8] Omsop project (optimised microturbine solar power system), https://cordis.europa.eu/project/id/308952, accessed: 2021-10-26.

[9] "MTT - EnerTwin Datasheet", https://enertwin.com/enertwin-specifications/, accessed: 2021-07-11.

[10] "A400 Datasheet", https://aureliaturbines.com/products, accessed: 2021-07-11.

[11] G. Tilocca, D. Sánchez, M. Torres García, Root cause analysis of the lack of market success of micro gas turbine systems, Turbo Expo: Power for Land, Sea, and Air.doi:https://doi.org/10.1115/GT2022-82146.

[12] A. Escamilla Perejón, D. T. Sánchez Martínez, L. García Rodríguez, Assessment of power-to-power renewable energy storage based on the smart integration of hydrogen and micro gas turbine technologies, International Journal of Hydrogen Energy, 47 (40), 17505-17525.doi:https://doi.org/10.1016/j.ijhydene.2022.03.238.

[13] D. Sánchez, M. Rollán, L. García-Rodríguez, G. Martínez, Solar Desalination Based on Micro Gas Turbines Driven by Parabolic Dish Collectors, Journal of Engineering for Gas Turbines and Power 142. doi:https://doi.org/10.1115/1.4045474.

[14] J. Montes-Sánchez, B. de Weert, B. Petit, L. García-Rodríguez, D. Sánchez, Potential of Micro Gas Turbines to Provide Renewable Heat and Power in Off-Grid Applications for Desalination and Industrial Wastewater Treatment, in: ASME (Ed.), ASME Turbo Expo, Virtual-Online, 2021. doi:https://doi.org/10.1115/GT2021-60253.

[15] R. González-Almenara, P. Rodríguez de Arriba, F. Crespi, D. Sánchez, A. Muñoz, T. Sánchez-Lencero, Supercritical carbon dioxide cycles for concentrated solar power plants: A possible alternative for solar desalination, Processes 10 (1) (2021) 72. doi:https://doi.org/10.3390/pr10010072.

[16] B. Petit, E. Sánchez-Carceller, J. Montes-Sánchez, R. González-Almenara, D. Sánchez, Market opportunities of water treatments powered by solar micro gas turbines: Chile and ecuador case studies, Processes 10 (3) (2022) 556. doi:https://doi.org/10.3390/pr10030556.

[17] A. Giostri, Preliminary analysis of solarized micro gas turbine application to csp parabolic dish plants, Energy Procedia 142 (2017) 768–773. doi:https://doi.org/10.1016/j.egypro.2017.12.124.
[18] F. Alnaimat, M. Ziauddin, B. Mathew, A review of recent advances in humidification and dehumidification desalination technologies using solar energy, Desalination 499 (2021) 114860. doi:https://doi.org/10.1016/j.desal.2020.114860.
[19] A. M. Delgado-Torres, L. García-Rodríguez, Solar desalination driven by organic rankine cycles (orc) and supercritical co2 power cycles: An update, Processes 10 (1) (2022) 153. doi:https://doi.org/10.3390/pr10010153.
[20] L. García-Rodríguez, A. M. Delgado-Torres, Renewable energy-driven desalination: New trends and future prospects of small capacity systems, Processes 10 (4) (2022) 745.
[21] R. L. Stover, Seawater reverse osmosis with isobaric energy recovery devices, Desalination 203 (1-3) (2007) 168–175. doi:https://doi.org/10.1016/j.desal.2006.03.528.
[22] MATLAB, version R2022a, The MathWorks Inc., Natick, Massachusetts, 2022.
[23] I. H. Bell, J. Wronski, S. Quoilin, V. Lemort, Pure and pseudo-pure fluid thermophysical property evaluation and the open-source thermophysical property library coolprop, Industrial & Engineering Chemistry Research 53 (6) (2014) 2498–2508. doi:10.1021/ie4033999.
[24] A. Razak, Industrial Gas Turbine: Performance Operability, 2007. doi:10.1533/9781845693404.
[25] M. H. Sharqawy, J. H. Lienhard, S. M. Zubair, Thermophysical properties of seawater: a review of existing correlations and data, Desalination and water Treatment 16 (1-3) (2010) 354–380. doi:https://doi.org/10.5004/dwt.2010.1079.
[26] Q+ lg chem, `https://www.lgwatersolutions.com/en/tools/software`, accessed: 2022-07-13.
[27] R. Aungier, Centrifugal Compressors: A Strategy for Aerodynamic Design and Analysis, ASME Press, 2000. doi:https://doi.org/10.1115/1.800938.
[28] F. Wiesner, A review of slip factors for centrifugal impellers, ASME, J. Eng. Power 89 (4) (1967) 158–566. doi:10.1115/1.3616734.
[29] D. Japikse, Centrifugal compressor design and performance, Concepts Eti, 1996.
[30] A. Egli, et al., The leakage of steam through labyrinth seals, Trans. Asme 57 (3) (1935) 115–122.
[31] R. Nece, J. Daily, Roughness effects on frictional resistance of enclosed rotating disksdoi:https://doi.org/10.1115/1.3662656.
[32] A. Sayma, D. Iaria, M. Khader, J. Al Zaili, Multi-objective optimisation of a centrifugal compressor for a micro gas turbine operated by concentrated solar power, in: Proceedings of the Global Power and Propulsion Forum 2017, 2017.
[33] T. Mancini, P. Heller, B. Butler, B. Osborn, W. Schiel, V. Goldberg, R. Buck, R. Diver, C. Andraka, J. Moreno, Dish-stirling systems: An overview of development and status, Journal of Solar Energy Engineering-transactions of The Asme - J SOL ENERGY ENG 125. doi:10.1115/1.1562634.
[34] H. J. Strumpf, D. M. Kotchick, M. G. Coombs, High-Temperature Ceramic Heat Exchanger Element for a Solar Thermal Receiver, Journal of Solar Energy Engineering 104 (4) (1982) 305–309. doi:https://doi.org/10.1115/1.3266322.
[35] W. Wang, G. Ragnolo, L. Aichmayer, T. Strand, B. Laumert, Integrated design of a hybrid gas turbine-receiver unit for a solar dish system, Energy Procedia 69 (2015) 583–592, international Conference on Concentrating Solar Power and Chemical Energy Systems, SolarPACES 2014. doi:https://doi.org/10.1016/j.egypro.2015.03.067.
[36] L. Aichmayer, J. Spelling, B. Laumert, Preliminary design and analysis of a novel solar receiver for a micro gas-turbine based solar dish system, Solar Energy 114 (2015) 378–396. doi:https://doi.org/10.1016/j.solener.2015.01.013.
[37] Optimized dish design, omsop project, `https://etn.global/wp-content/uploads/2019/02/D1.5-Optimized-dish-design.pdf`, accessed: 2021-10-26 (2015).
[38] W. Wang, Development of an Impinging Receiver for Solar Dish-Brayton Systems (PhD dissertation), KTH Royal Institute of Technology, Stockholm, 2015.
[39] W. Wang, H. Xu, B. Laumert, T. Strand, An inverse design method for a cavity receiver used in solar dish brayton system, Solar energy 110 (2014) 745–755. doi:https://doi.org/10.1016/j.solener.2014.10.019.
[40] W. Wang, B. Laumert, H. Xu, T. Strand, Conjugate heat transfer analysis of an impinging receiver design for a dish-brayton system, Solar Energy 119 (2015) 298–309. doi:https://doi.org/10.1016/j.solener.2015.07.013.
[41] M. Uzair, T. N. Anderson, R. J. Nates, Modeling of convective heat loss from a cavity receiver coupled to a dish concentrator, Solar Energy 176 (2018) 496 – 505. doi:https://doi.org/10.1016/j.solener.2018.10.060.
[42] M. L. Ferrari, U. M. Damo, A. Turan, D. Sánchez, Hybrid systems based on solid oxide fuel cells: modelling and design, John Wiley & Sons, 2017.
[43] C. F. McDonald, Low-cost compact primary surface recuperator concept for microturbines, Applied Thermal Engineering 20 (5) (2000) 471–497. doi:10.1016/S1359-4311(99)00033-2.
[44] C. F. McDonald, A. F. Massardo, C. Rodgers, A. Stone, Recuperated gas turbine aeroengines, part ii: engine design studies following early development testing, Aircraft Engineering and Aerospace Technologydoi:10.1108/00022660810873719.
[45] C. F. McDonald, Recuperator considerations for future higher efficiency microturbines, Applied Thermal Engineering 23 (12) (2003) 1463–1487. doi:https://doi.org/10.1016/S1359-4311(03)00083-8.
[46] G. Xiao, T. Yang, H. Liu, D. Ni, M. L. Ferrari, M. Li, Z. Luo, K. Cen, M. Ni, Recuperators for micro gas turbines: A review, Applied Energy 197 (2017) 83–99. doi:https://doi.org/10.1016/j.apenergy.2017.03.095.
[47] G. Nellis, S. Klein, Heat transfer, Cambridge university press, 2008.
[48] K. Hoopes, D. Sánchez, F. Crespi, A new method for modelling off-design performance of sco2 heat exchangers without specifying detailed geometry, in: Fifth Supercritical CO2 Power Cycles Symposium, 2016.
[49] F. Crespi, D. Sánchez, K. Hoopes, B. Choi, N. Kuek, The conductance ratio method for off-design heat exchanger modeling and its impact on an sco2 recompression cycle, in: Turbo Expo: Power for Land, Sea, and Air, Vol. 50961, American Society of Mechanical Engineers, 2017. doi:https://doi.org/10.1115/GT2017-64908.
[50] T. Neises, Steady-state off-design modeling of the supercritical carbon dioxide recompression cycle for concentrating solar power applications with two-tank sensible-heat storage, Solar Energy 212 (2020) 19–33. doi:https://doi.org/10.1016/j.solener.2020.10.041.
[51] F. Crespi, D. Sánchez, T. Sánchez, G. S. Martínez, Capital cost assessment of concentrated solar power plants based on supercritical carbon dioxide power cycles, Journal of Engineering for Gas Turbines and Power 141 (7). doi:https://doi.org/10.1115/1.4042304.

[52] R. Aungier, Turbine Aerodynamics: Axial-flow and Radial-inflow Turbine Design and Analysis, ASME Press, 2006. doi:https://doi.org/10.1115/1.802418.
[53] LG SW 440 GR datasheet, https://www.lgwatersolutions.com/en/product/seawater-ro/LG-SW-440-GR, accessed: 2022-07-13.
[54] A. Panagopoulos, K.-J. Haralambous, M. Loizidou, Desalination brine disposal methods and treatment technologies-a review, Science of the Total Environment 693 (2019) 133545. doi:https://doi.org/10.1016/j.scitotenv.2019.07.351.
[55] R. Xiong, C. Wei, Current status and technology trends of zero liquid discharge at coal chemical industry in china, Journal of Water Process Engineering 19 (2017) 346–351. doi:https://doi.org/10.1016/j.jwpe.2017.09.005.
[56] M. Elimelech, W. A. Phillip, The future of seawater desalination: energy, technology, and the environment, science 333 (6043) (2011) 712–717. doi:10.1126/science.1200488.
[57] M. Yaqub, W. Lee, Zero-liquid discharge (zld) technology for resource recovery from wastewater: A review, Science of the total environment 681 (2019) 551–563. doi:https://doi.org/10.1016/j.scitotenv.2019.05.062.
[58] W. Song, L. Y. Lee, E. Liu, X. Shi, S. L. Ong, H. Y. Ng, Spatial variation of fouling behavior in high recovery nanofiltration for industrial reverse osmosis brine treatment towards zero liquid discharge, Journal of Membrane Science 609 (2020) 118185. doi:https://doi.org/10.1016/j.memsci.2020.118185.
[59] G. U. Semblante, J. Z. Lee, L. Y. Lee, S. L. Ong, H. Y. Ng, Brine pre-treatment technologies for zero liquid discharge systems, Desalination 441 (2018) 96–111. doi:https://doi.org/10.1016/j.desal.2018.04.006.
[60] E. Sánchez Carceller, Concentrate treatments in reverse osmosis desalination plants: Status and innovative proposals, https://idus.us.es/handle/11441/108816 (2020).
[61] J. Remund, S. Müller, S. Kunz, C. Schilter, Meteonorm v7 handbook part i: Software, Number May (2012) 39.
[62] M. Wilf, L. Awerbuch, The guidebook to membrane desalination technology: reverse osmosis, nanofiltration and hybrid systems: process, design, applications and economics, Balaban Desalination Publications, 2007.
[63] R. González-Almenara, A. Muñoz, D. Sánchez, Commercial availability of micro gas turbines, http://institucional.us.es/solmideff/ (2020).